J. Fluid Mech. (2004), *vol.* 503, *pp.* 201–245. © 2004 Cambridge University Press
DOI: 10.1017/S0022112004007876 Printed in the United Kingdom

An approach to entropy consistency in second-order hydrodynamic equations

By RAMESH BALAKRISHNAN†

Center for Simulation of Advanced Rockets, University of Illinois at Urbana–Champaign, Illinois 61801, USA

(Received 6 June 2001 and in revised form 9 October 2003)

As the flow becomes rarefied it has been seen that predictions of continuum formulations, such as the Navier–Stokes equations, become inaccurate. These inaccuracies stem from the linear approximations to the stress and heat flux in the viscous flux terms in the Navier–Stokes equations. Hence, it has long been conjectured that the inclusion of higher-order terms in the constitutive relations for the stress and heat flux may improve the predictive capabilities of such continuum formulations. Following this approach, second-order systems of hydrodynamic equations, such as the Burnett and Woods equations, were applied to the shock structure problem. While it was observed that these equations afforded a better description of the shock structure on coarse grids, they were prone to small wavelength instabilities when the grids were refined. The cause of this instability was subsequently traced to the fact that these equations can potentially violate the second law of thermodynamics when the local Knudsen number exceeds a critical limit. This leads to the fundamental question: is entropy consistency achievable in a system of second-order hydrodynamic equations? To answer this question, a novel set of equations, known as the BGK-Burnett equations, is constructed by taking moments of the Boltzmann equation for the second-order distribution function.

The formulation of second-order hydrodynamic equations by moment methods is beset by three hurdles: (i) the highly nonlinear collision integral in the Boltzmann equation needs to be evaluated, (ii) the second-order distribution function does not satisfy the moment closure criterion and (iii) identification of the approximations to the material derivatives in the second-order distribution function that will correctly account for the difference in time scales between the first- and second-order fluxes. The first three terms of the Chapman–Enskog expansion, that defines the second-order distribution function, and the Bhatnagar–Gross–Krook model of the collision integral, form the basis of the BGK-Burnett equations. The entropy-consistent behaviour of the equations depend on the moment closure coefficients and the approximations to the material derivatives in the second-order fluxes. The requirement of moment closure alone, however, results in non-unique closure coefficients and a family of BGK-Burnett equations, from which an entropy-consistent set must be identified. From this family, two sets of BGK-Burnett equations have been considered, and this paper presents the details of the formulation of these two sets of equations, the identification of entropy-consistent approximations to the material derivatives by a novel entropy consistent relaxation technique, and shock

† Present address: National Center for Supercomputing Applications, 152 Computing Applications Building, 605 West Springfield Avenue, Champaign, Illinois 61820, USA.

https://doi.org/10.1017/S0022112004007876 Published online by Cambridge University Press

structure computations in a monatomic hard sphere gas for a range of Mach numbers.

1. Introduction

The classification of the various flow regimes is based on a dimensionless parameter, known as the Knudsen number, which is a measure of the degree of rarefaction of the medium. The Knudsen number Kn is defined as the ratio of the mean free path and a characteristic length (i.e. $Kn = \lambda / L_{ref}$) where λ denotes the mean free path between molecular collisions and L_{ref} denotes the characteristic length of the geometry (e.g. the nose radius of a blunt body). At standard sea level conditions, for air, $\lambda \approx 7.25 \times 10^{-8}$ m and the gas is said to be in the continuum regime. The Knudsen number in this regime, for most aerodynamic applications, is much less than unity. Collisions between gas molecules are numerous and the gas can be considered to be in thermodynamic equilibrium.

At an altitude greater than 150 km, where the density is much lower, the free-stream Knudsen number is much greater than unity. This regime is known as the free molecular regime. Collisions between molecules are so infrequent that they can be neglected to a good approximation. The only collisions that need be considered are those between the molecules and solid boundaries. Modelling flows in this regime calls for a solution of the Boltzmann equation or a simulation of the same using the Direct Simulation Monte Carlo (DSMC) technique (see Bird 1994).

In the continuum–transition flow regime, which lies between the extremes of the continuum and free molecular regimes, the Knudsen number is in the neighbourhood of unity. The Navier–Stokes equations yield inaccurate results, as the approximations made in the constitutive relations for the stress and heat flux terms, which are acceptable in the continuum regime, are not appropriate in the transitional regime. The insufficient number of collisions between the molecules prevents the gas from attaining thermodynamic equilibrium. This gives rise to regions of non-equilibrium where more general constitutive relations are required to model the flow. To complicate matters even further, there may be regions of continuum and rarefaction that occur side by side. An example of this is the flow field around orbital transfer vehicles (OTV) when they re-enter the upper atmosphere. For certain altitudes, the flow field close to the fore-body region can be represented as a continuum, while the wake region exhibits a high degree of rarefaction. Also, the small radii of curvature associated with the cowl lip and nose cone geometries are characterized by high local Knudsen numbers although the local Knudsen numbers may be in the continuum regime for much of the remaining portions of the body.

While the flow in the continuum and rarefied regimes can be simulated to a high degree of accuracy with computational fluid dynamics (CFD) solvers and DSMC techniques, respectively, there are problems associated with the use of any one of these computational tools alone in the continuum–transition regime (see Boyd, Chen & Candler 1995). In this regime, the linear constitutive relations in the stress and heat flux in the Navier–Stokes equations have been shown to yield inaccurate results. Also, the large number of molecules required for meaningful results in the continuum–transition regime makes the DSMC technique prohibitively expensive with regard to computational time and storage requirements. Hence, it was conjectured that an extended set of governing equations, which incorporates more general expressions for

https://doi.org/10.1017/S0022112004007876 Published online by Cambridge University Press

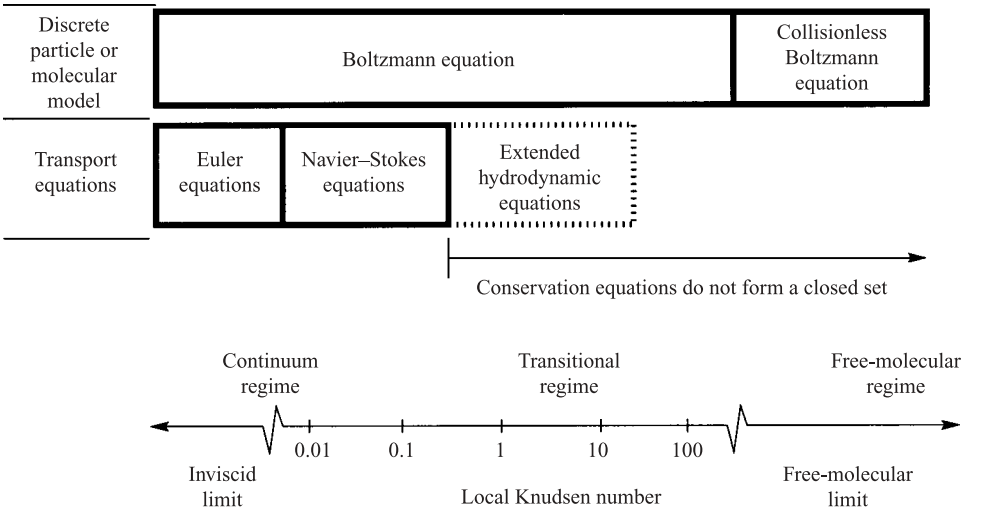


FIGURE 1. The Knudsen number limits on the conventional mathematical models of neutral gas flows. Adapted from Moss & Bird (1984).

the constitutive relations, may extend the limits of applicability of the Navier–Stokes equations. On including these new constitutive relations in traditional CFD solvers (Navier–Stokes solvers in the continuum domain) it may be expected that in addition to capturing the intricacies of the flow field they will also prove to be computationally faster than Monte Carlo simulations.

1.1. *Moment methods and higher-order hydrodynamic equations*

One of the techniques for deriving higher-order constitutive relations is by the method of moments. The idea behind this method is to formulate higher-order distribution functions that describe the velocity (and internal energy) distribution over the entire phase space. Moments of the Boltzmann equation, for the higher-order distribution function, with the collision invariant vector give rise to an extended set of hydrodynamic equations.

The Chapman–Enskog technique develops the higher-order distribution function as a perturbative expansion about the equilibrium (Maxwellian) distribution with the Knudsen number as the perturbation parameter. The Knudsen number is assumed to be less than unity and each successive approximation to the distribution function is proportional to successive powers of the Knudsen number. The higher-order approximations are found by substituting the expansion in the non-dimensionalized Boltzmann equation and equating terms that have like powers of the Knudsen number. One of the advantages of using the Chapman–Enskog expansion is that it does not introduce additional hydrodynamic variables or transport equations into the system of hydrodynamic equations. Moments of the Boltzmann equation for the first three terms of the Chapman–Enskog expansion, which define the second-order distribution function, give rise to the Burnett equations. Beyond the first-order, this expansion augments the stress and heat flux expressions in the Navier–Stokes equations with terms that contain higher-order derivatives and products of derivatives. A fundamental difficulty associated with such a formulation is that they do not satisfy the moment closure property for distribution functions beyond the first-order. Consequently, the resulting higher-order hydrodynamic equations do not form a closed set, as shown in figure 1. The moment closure property requires that moments

https://doi.org/10.1017/S0022112004007876 Published online by Cambridge University Press

of the higher-order terms with the collision invariant vector vanish. This, in other words, means that the field vector of the hydrodynamic equations, which consists of the mass, momentum and total energy, remains the same for any system of governing equations derived by this methodology. In order to satisfy this requirement, additional terms, that are suitably weighted, are introduced to obtain closed-form expressions. This introduces a certain degree of arbitrariness in the formulations which leads to non-uniqueness in the magnitudes of the coefficients of the additional terms in the second-order distribution function.

1.2. *Burnett computations: successes and drawbacks*

The work done by Fiscko & Chapman (1988), Zhong (1991) and Welder, Chapman & MacCormack (1993) aimed at solving the time-dependent Burnett equations by approximating the material derivatives in the second-order fluxes and using numerical techniques developed for solving the time-dependent Navier–Stokes equations. This approach extended the numerical methods for continuum flow into the continuum–transition regime by including the Burnett expressions for stress and heat flux into standard Navier–Stokes solvers. In one of the earliest successful computations of the Burnett equations, Fiscko & Chapman (1988) used the Euler approximations to the material derivatives (see Chapman & Cowling 1970) and solved the hypersonic shock structure problem for a monatomic hard sphere gas and argon. The shock structure solutions, obtained on coarse grids for a wide range of Mach numbers, showed that the Burnett equations describe the shock structure better than the Navier–Stokes equations. The Burnett solutions were in close agreement with the results obtained from Monte Carlo simulations and experimental measurements (see Alsmeyer 1976). However, grid refinement studies indicated that the Burnett equations became unstable as the mesh size was made progressively finer. This was predicted by Bobylev (1982) who showed that the linearized Burnett equations are unstable to small wavelength disturbances. This instability made it impossible to obtain Burnett solutions for complex three-dimensional flows above a certain altitude.

In an effort to overcome these instabilities, Zhong (1991) showed that the Burnett equations could be stabilized by adding linear third-order terms from the super-Burnett equations. This set of equations was termed the augmented Burnett equations. The weights (coefficients) of these linear third-order terms were determined by a linearized stability analysis of the augmented Burnett equations. The augmented Burnett equations did not present stability problems when they were used to compute the hypersonic shock structure and hypersonic blunt-body flows. Their predictions of the hypersonic flow field were in agreement with DSMC computations in the continuum–transition regime (see Zhong & Furumoto 1995; Agarwal, Yun & Balakrishnan 2001). However, attempts at computing blunt-body wakes and flat-plate boundary layers even with the augmented Burnett equations have not been entirely successful. Complex hypersonic flow fields like those in the aft region of hypersonic bodies (see Lumpkin 1990) and shock cowl lip interactions could not be computed successfully with the augmented Burnett equations. It was also observed that the augmented Burnett equations could orient the flow in a physically unrealistic manner by allowing shear layers to sharpen to discontinuities and permitting heat flow from cold to hot regions. Since this solution violates the second-law of thermodynamics, it was conjectured that an inherent entropy inconsistency may be the cause of the computational instability. Following this line of reasoning, a rigorous thermodynamic analysis of the Burnett equations ensued, where it was shown by Comeaux (1995) that the one-dimensional Burnett equations, when applied to the hypersonic shock

https://doi.org/10.1017/S0022112004007876 Published online by Cambridge University Press

structure problem, can violate the second law of thermodynamics as the local Knudsen number increases above a critical limit.

Since the improperly modelled material derivatives in the higher-order stress and heat flux give rise to instabilities that make the equations inconsistent with the second law of thermodynamics, Jin, Pareschi & Slemrod (2002) and Jin & Slemrod (2001) have proposed an algorithmic approach that develops relaxation equations for the evolution of the stress and heat flux. The resulting relaxed Burnett system of equations consists of the gas dynamic equations for the conserved variables and the equations for the stress and heat flux. Since the stress and heat flux are not conserved quantities, their evolution with standard shock capturing schemes for the conserved variables is not possible. In addition, the time scale for the stress and heat flux are faster than the time scales for the conserved variables, making the relaxed Burnett equations stiff. While the relaxed Burnett equations are reported to give more accurate results than the extended thermodynamic approximations and the Navier–Stokes equations, the operator split schemes (see Jin *et al.* 2002) used to solve them appear to place restrictions on the CFL condition.

Another approach by Al-Ghoul & Eu (2001), which is not based on kinetic theory, develops evolution equations for the stress and heat flux on a phenomenological basis. These evolution equations together with the gas dynamic equations for the conserved variables constitute the set of generalized hydrodynamics equations. By introducing the adiabatic approximation that assumes that the stress and heat flux are in the steady state on the time scales of the conserved variables, they have obtained shock solutions that compare well with experimental results. Since this approach does not have an H-theorem, they have used *calotropy* production as a measure of entropy consistency and shown solutions for a range of Mach numbers by integrating the stiff ordinary differential equations. While it is rational to expect the non-conserved variables to be in steady state on the time scales of the conserved variables and approximate the material derivatives by their steady-state values, it has been shown (see Welder *et al.* 1993) that for the Burnett and Woods equations, this approximation creates an unphysical heat flux at the leading edge of the shock. As a result, the temperature could drop to zero at the leading edge of the shock thereby causing the equations to fail.

1.3. *Motivation for a novel formulation*

While the work of Comeaux (1995) demonstrated that the Burnett equations can violate the second-law of thermodynamics under certain conditions, it was still not clear what factors gave rise to negative irreversible entropy production. Such unphysical effects could arise because the higher-order hydrodynamic equations do not form a closed set. Also, as mentioned earlier, the Burnett coefficients were derived for Maxwellian and hard sphere gas models. For a real gas, the coefficients were assumed to lie between these two extremes and were determined using an interpolation scheme devised by Lumpkin (1990). Further, it was noticed by the author (see Balakrishnan 1999) that although the Burnett equations did take into account the influence of forces between molecules (appropriately modelled) it did not incorporate the corresponding higher-order virial expansion for the equation of state. In all prior attempts at computing the Burnett equations, the ideal gas law had been assumed. This, perhaps, was the reason for the increased instability with the Maxwellian gas as compared to the hard sphere gas (see Fiscko & Chapman 1988; Zhong 1991). Another cause for such unphysical effects lies in the improper approximation to the material derivatives in the second-order stress and heat flux

https://doi.org/10.1017/S0022112004007876 Published online by Cambridge University Press

terms. While the Euler approximation is found to be appropriate for the material derivatives in the first-order terms, it remains, as yet, unknown what approximation may account for the difference in relaxation times between the first- and second-order fluxes.

Based on these observations, the formulation of the BGK-Burnett equations was pursued with the objective of developing a system of entropy-consistent second-order hydrodynamic equations for a monatomic hard sphere gas where there is no force field between the constituent molecules. The formulation proceeds by deriving the second-order distribution function by considering the first three terms of the Chapman–Enskog expansion and using the Bhatnagar–Gross–Krook (BGK) model for the collision integral. It has been shown (see Balakrishnan & Agarwal 1997; Balakrishnan, Agarwal & Yun 1999) that the mere requirement of moment closure generates a family of BGK-Burnett equations. The behaviour of these equations depends on the closure coefficients as well as the approximations to the material derivatives in the second-order fluxes. Consequently, given a set of equations belonging to this family, the task of formulating an entropy-consistent set of equations is one of identifying entropy-consistent approximations to the material derivatives. The entropy-consistent approximations are identified by a novel entropy-consistent relaxation technique. This approach is different from that of Al-Ghoul & Eu (2001) and Jin *et al.* (2002) in that there are no additional equations for the evolution of the stress and heat flux and it is not algorithmic. Instead, the aim of this work is to develop equations by approximating the material derivatives to account for the difference in time scales betwen the first- and second-order fluxes in an entropy-consistent manner.

For second- and higher-order departures from equilibrium, it is well known that the Chapman–Enskog expansion destroys the frame invariant property. In particular, it has been shown that the Burnett equations are not invariant to rotational transformations (see Muller 1972). While there are other equations (see Woods 1993) that correct this, the formulation and analysis of the BGK-Burnett equations presented in this paper is confined to solving the one-dimensional shock structure problem where there is no vorticity; as a consequence of which the problems (and errors) associated with the frame-dependent terms that arise in the computation of shear layers with higher-order hydrodynamic equations in two and three spatial dimensions are circumvented.

1.4. *Outline of the paper*

The structure of the paper is as follows. Section § 2 describes the formulation of the second-order hydrodynamic equations known as the BGK-Burnett Model 1 equations. The Model 1a and Model 1b second-order stress and heat flux are derived by neglecting and retaining, respectively, the material and spatial derivatives of the collision frequency, and the expressions for the stress and heat flux are compared with the Burnett and Woods equations. Section § 3 explores the need for approximating the material derivatives in the second-order flux by presenting the linearized stability analysis of the Model 1 equations. Section § 4 describes shock structure computations using the Model 1a and Model 1b equations and identifies the fictitious viscosity that causes the Model 1a equations to become unstable as the grids are refined. Section § 5 describes the Boltzmann's H-theorem and the formulation of the expression for the irreversible entropy production in the second-order equations. It is shown that the Model 1b equations produce negative irreversible entropy at medium Mach numbers as the grid fineness ratio is reduced. Section § 6 describes the approach to identify entropy-consistent BGK-Burnett equations by using the novel entropy-consistent

https://doi.org/10.1017/S0022112004007876 Published online by Cambridge University Press

relaxation technique and the results of this approach when applied to the Model 1b equations. Section § 7 presents the formulation of the Model 2 equations with the additional constraint that the linearized Model 2 and linearized Navier–Stokes equations have similar stability characteristics. It is demonstrated that the Model 2b equations are entropy-consistent. Shock structures for free-stream Mach numbers 1.2, 5, 10 and 20 are computed with the Model 2b equations and the shock profiles and shock thickness are compared with results obtained from DSMC computations and with experimental data. Section § 8 presents the conclusions and summarizes the main findings of this work.

2. Distribution functions

A molecule is characterized by its position $\boldsymbol{r}$, velocity $\boldsymbol{v}$ and internal energy ϵ which together constitutes a seven-dimensional phase space. The simplest function that contains this information, at any given instant of time, is the distribution function. Mathematically speaking, the distribution function expresses the probability of finding molecules in the physical volume d^3r whose velocities and internal energy lie in the range $\boldsymbol{v}$ to $\boldsymbol{v}+\mathrm{d}\boldsymbol{v}$ and ϵ to $\epsilon+\mathrm{d}\epsilon$, respectively. Such molecules are said to belong to the class $\mathscr{C}(\boldsymbol{v},\epsilon)$. The number density or expected number of such molecules per unit volume is defined as

$$n(\boldsymbol{r},t)=\int_{\mathbb{R}^3}\int_{\mathbb{R}^+}\mathscr{F}(t,\boldsymbol{r},\boldsymbol{v},\epsilon)\,\mathrm{d}^3v\,\mathrm{d}\epsilon \tag{2.1}$$

where $\mathbb{R}=(-\infty,\infty)$, $\mathbb{R}^+=[0,\infty)$ and the distribution function is given by the mapping

$$\mathscr{F}=\mathscr{F}(t,\boldsymbol{r},\boldsymbol{v},\epsilon):\mathbb{R}^+\times\mathbb{R}^3\times\mathbb{R}^3\times\mathbb{R}^+\to\mathbb{R}^+. \tag{2.2}$$

The flow variables that are described by the hydrodynamic equations are averages of quantities that depend on the velocity and internal energy of the constituent molecules. These averages are defined as moments of the distribution function.

Definition. *The moment of a function,* $\phi=\phi(t,\boldsymbol{v},\epsilon):\mathbb{R}^+\times\mathbb{R}^3\times\mathbb{R}^+\to\mathbb{R}$, *is defined as the inner product*

$$\bar{\phi}(\boldsymbol{r},t)=\langle\phi(\boldsymbol{v},\epsilon),f(t,\boldsymbol{r},\boldsymbol{v},\epsilon)\rangle=\int_{\mathbb{R}^3}\int_{\mathbb{R}^+}\phi(t,\boldsymbol{v},\epsilon)f(t,\boldsymbol{r},\boldsymbol{v},\epsilon)\,\mathrm{d}^3v\,\mathrm{d}\epsilon, \tag{2.3}$$

where, the distribution function is normalized as

$$f(t,\boldsymbol{r},\boldsymbol{v},\epsilon)=\frac{\mathscr{F}(t,\boldsymbol{r},\boldsymbol{v},\epsilon)}{n(\boldsymbol{r},t)} \tag{2.4}$$

such that

$$\langle f(t,\boldsymbol{r},\boldsymbol{v},\epsilon)\rangle=\int_{\mathbb{R}^3}\int_{\mathbb{R}^+}f(t,\boldsymbol{r},\boldsymbol{v},\epsilon)\,\mathrm{d}^3v\,\mathrm{d}\epsilon=1. \tag{2.5}$$

If the gas is assumed to be composed of a single species of identical molecules, then in the absence of external forces, the Boltzmann equation which expresses the number conservation of the gas molecules is given by

$$\left(\frac{\partial}{\partial t}+\boldsymbol{v}\cdot\nabla_{\boldsymbol{r}}\right)\rho f=\left[\frac{\mathrm{d}\rho(\boldsymbol{r},t)}{\mathrm{d}t}\right]_{\mathrm{coll}}=J[f(\boldsymbol{v},\epsilon),f(\boldsymbol{v}_1,\epsilon_1)] \tag{2.6}$$

https://doi.org/10.1017/S0022112004007876 Published online by Cambridge University Press

where the collisions integral, $J[f(\boldsymbol{v},\epsilon), f(\boldsymbol{v}_1,\epsilon_1)]$, is given by (see Vincenti & Kruger 1965)

$$\int_{\mathbb{R}^+}\int_{\mathbb{R}^3}\int_0^{4\pi} \rho^2[f(\boldsymbol{v}',\epsilon')f(\boldsymbol{v}_1',\epsilon_1') - f(\boldsymbol{v},\epsilon)f(\boldsymbol{v}_1,\epsilon_1)]g\sigma\,\mathrm{d}\omega\,\mathrm{d}^3v_1\,\mathrm{d}\epsilon_1, \tag{2.7}$$

where $\rho(\boldsymbol{r},t)$ is the density of the gas, $\boldsymbol{g}=\boldsymbol{v}_1-\boldsymbol{v}$ is the relative velocity vector between the colliding pairs and $\sigma\,\mathrm{d}\omega$ denotes the collision cross-section. The primed variables denote post-collisional values. The collision integral represents the rate of change of the number of molecules due to two competing collision processes: direct collisions between molecules of classes $\mathscr{C}(\boldsymbol{v},\epsilon)$ and $\mathscr{C}_1(\boldsymbol{v}_1,\epsilon_1)$ that deplete the number of molecules in $\mathscr{C}(\boldsymbol{v},\epsilon)$ and inverse collisions between molecules of $\mathscr{C}'(\boldsymbol{v}',\epsilon')$ and $\mathscr{C}_1'(\boldsymbol{v}_1',\epsilon_1')$ that replenish the number of molecules in $\mathscr{C}(\boldsymbol{v},\epsilon)$. The collision integral is a function of $\boldsymbol{v}$ and ϵ after the integrations over $\boldsymbol{v}_1$ and ϵ_1 are carried out.

By setting the kernel of the collision integral equal to zero we obtain

$$\log_{\mathrm{e}} f(\boldsymbol{v}',\epsilon') + \log_{\mathrm{e}} f(\boldsymbol{v}_1',\epsilon_1') = \log_{\mathrm{e}} f(\boldsymbol{v},\epsilon) + \log_{\mathrm{e}} f(\boldsymbol{v}_1,\epsilon_1), \tag{2.8}$$

which expresses the conservation of physical variables during the collision process. These physical variables, also known as collision variables, are readily seen to be the mass, momentum and total energy of the colliding pairs of molecules. By considering the conservation of total energy (see Deshpande 1986), as opposed to conservation of translational kinetic energy alone, it is theoretically possible to extend the definition of the distribution function to polyatomic gases. In practice, however, such an extension must account for the time lag in the transfer of energy from the translational mode to the internal degrees of freedom. The Maxwellian distribution function for one-dimensional hydrodynamic flows is given by

$$f^{(0)} = \frac{\rho}{I_0}\sqrt{\frac{\beta}{\pi}}\,\exp(-I/I_0)\,\exp\!\left(-\beta C_x^2\right) \tag{2.9}$$

where $I=\epsilon+v_x^2/2+v_y^2/2$, $\beta=1/2RT$, $C_x=v_x-u_x$ is the thermal or peculiar velocity and $I_0=\langle I, f^{(0)}\rangle$ denotes the average internal energy. Hereinafter, I will be referred to as the internal energy, although it must be understood that only in three-dimensional hydrodynamic equations is I equal to the actual internal energy ϵ (see Balakrishnan 1999). Throughout this paper the molecular, fluid and thermal velocity components will be denoted by (v_x,v_y,v_z), (u_x,u_y,u_z) and (C_x,C_y,C_z), respectively. It must be noted that such a notation does not represent partial derivatives with respect to the subscripted variable. The variables that are conserved in a collision process define the collision invariant vector,

$$\boldsymbol{\Psi} = \left[1,\, v_x,\, I+\tfrac{1}{2}\,v_x^2\right]^{\mathrm{T}}. \tag{2.10}$$

From here on, the density of the gas $\rho(\boldsymbol{r},t)$ has been absorbed in the expression for the distribution function as a result of which $\langle f\rangle=\rho$. The collision integral satisfies the relation

$$\langle \boldsymbol{\Psi},\, J[f(\boldsymbol{v},I), f(\boldsymbol{v}_1,I_1)]\rangle = 0, \tag{2.11}$$

thereby indicating that the corresponding collision variables in the macroscopic scale are conserved too. By taking moments of the Boltzmann equation for the Maxwellian distribution function

$$\frac{\partial}{\partial t}\left\langle \boldsymbol{\Psi},\, f^{(0)}\right\rangle + \frac{\partial}{\partial x}\left\langle v_x\boldsymbol{\Psi},\, f^{(0)}\right\rangle = 0 \tag{2.12}$$

https://doi.org/10.1017/S0022112004007876 Published online by Cambridge University Press

we obtain the Euler equations

$$\frac{\partial \boldsymbol{Q}}{\partial t} + \frac{\partial \boldsymbol{G}^i}{\partial x} = 0 \tag{2.13}$$

where the field vector $\boldsymbol{Q} = \langle \boldsymbol{\Psi}, f^{(0)} \rangle$ and inviscid flux vector $\boldsymbol{G}^i = \langle v_x \boldsymbol{\Psi}, f^{(0)} \rangle$ are given by

$$\boldsymbol{Q} = \begin{pmatrix} \rho \\ \rho u_x \\ \rho e_t \end{pmatrix}, \quad \boldsymbol{G}^i = \begin{pmatrix} \rho u_x \\ p + \rho u_x^2 \\ p u_x + \rho e_t u_x \end{pmatrix}.$$

2.1. *Bhatnagar–Gross–Krook (BGK) model and higher-order distribution functions*

In order to develop the Navier–Stokes and other higher-order hydrodynamic equations to model gas flows in conditions that are removed from collisional equilibrium, an expression for the corresponding distribution function is sought. The difficulties encountered in developing higher-order distribution functions are largely due to the highly nonlinear nature of the collision integral. Bhatnagar (1954) proposed a model equation to approximate the collision integral that reduces the mathematical complexity but retains many of its qualitative features. The BGK model equation is expressed as

$$J[f(\boldsymbol{v}, I), f(\boldsymbol{v}_1, I_1)] = \nu\big(f^{(0)} - f\big), \tag{2.14}$$

where $f^{(0)}$ is the local Maxwellian and ν is the collision frequency that may depend on the density and temperature, but is assumed to be independent of the molecular velocity $\boldsymbol{v}$. In this model equation, the depleting and replenishing collisions are assumed to be proportional to the collision frequency and the distribution function after collision obeys the local Maxwellian. This implies that any non-equilibrium distribution function decays to the local Maxwellian with a relaxation time equal to the reciprocal of the collision frequency. Owing to the presence of the local Maxwellian, the resulting Boltzmann equation (2.15) continues to be a nonlinear integro-differential equation. This is because $f^{(0)}$ depends on u_x and I_0 that are obtained as moments of the, as yet, unknown non-equilibrium distribution function f. The limitations of this model, as for instance a constant Prandtl number, $Pr = 1$, are well known and will be accepted with the knowledge that more sophisticated models for the collision integral can be constructed (see Holway 1965; Abe & Oguchi 1977) to overcome these inherent deficiencies. It suffices to say that the BGK model of the collision integral satisfies the minimum requirements of the Boltzmann equation: it has the required collision invariants that satisfy the moment property (2.11), it has an H-theorem and it reduces the non-equilibrium distribution function f to the Maxwellian distribution $f^{(0)}$ as time $t \to \infty$.

The one-dimensional Boltzmann equation with the BGK model for the collision integral is given by

$$\frac{\partial f}{\partial t} + v_x \frac{\partial f}{\partial x} = \nu\big(f^{(0)} - f\big). \tag{2.15}$$

On introducing the non-dimensional variables, $\hat{x} = x/L_{ref}$, $\hat{v}_x = v_x/C_{rms}$, $\hat{\nu} = (\nu\lambda)/C_{rms}$ and $\hat{t} = tC_{rms}/L_{ref}$, (2.15) reduces to the form

$$\xi\left(\frac{\partial f}{\partial \hat{t}} + \hat{v}_x \frac{\partial f}{\partial \hat{x}}\right) = \hat{\nu}\big(f^{(0)} - f\big), \tag{2.16}$$

where $\xi = \lambda/L_{ref}$ is the local Knudsen number. The local Knudsen number accounts for the scaling due to the difference in time scales between the streaming and

https://doi.org/10.1017/S0022112004007876 Published online by Cambridge University Press

collision operators in (2.15). The Chapman–Enskog expansion for the non-equilibrium distribution function is given by

$$f = f^{(0)} + \xi f^{(1)} + \xi^2 f^{(2)} + \cdots \tag{2.17}$$

where the higher-order terms in the distribution function, $f^{(i)}, \forall\, i = 1, 2, \ldots,$ are proportional to the corresponding power of ξ. Substituting (2.17) into (2.16) and equating like powers of the Knudsen number gives the following equation for the higher-order terms in the distribution function:

$$f^{(i)} = -\frac{1}{\xi \nu}\left(\frac{\partial}{\partial t} f^{(i-1)} + v_x \frac{\partial}{\partial x} f^{(i-1)}\right). \tag{2.18}$$

2.2. *First-order distribution function*

The first-order distribution function is obtained by considering the first two terms of the Chapman–Enskog expansion,

$$f = f^{(0)} + \xi f^{(1)} = f^{(0)}\big(1 + \xi \phi^{(1)}\big), \tag{2.19}$$

which on simplification (see Balakrishnan 1999) gives

$$f^{(1)} = -\frac{f^{(0)}}{\xi \nu}\left[\mathscr{A}^{(1)}(I, C_x)\frac{\partial \beta}{\partial x} + \mathscr{A}^{(2)}(I, C_x)\frac{\partial u_x}{\partial x}\right], \tag{2.20}$$

where

$$\left.\begin{aligned} \mathscr{A}^{(1)}(I, C_x) &= \frac{5}{2\beta} C_x - \frac{I}{\beta I_0} C_x - C_x^3, \\ \mathscr{A}^{(2)}(I, C_x) &= (3-\gamma)\beta C_x^2 - (\gamma - 1)\frac{I}{I_0} + \frac{(3\gamma - 5)}{2}. \end{aligned}\right\} \tag{2.21}$$

It can be shown that (2.20) and (2.21) readily satisfy the moment closure relation

$$\big\langle \boldsymbol{\Psi}, \xi^i f^{(i)} \big\rangle = 0, \forall\, i \geqslant 1. \tag{2.22}$$

The physical interpretation of (2.22) is that the higher-order terms in the distribution function do not add any additional terms to the field vector $\boldsymbol{Q}$ of the conservation equations. More importantly, the continuity equation remains unchanged. On taking moments of the Boltzmann equation for the first-order distribution function

$$\frac{\partial}{\partial t}\big\langle \boldsymbol{\Psi}, \big(f^{(0)} + \xi f^{(1)}\big)\big\rangle + \frac{\partial}{\partial x}\big\langle v_x \boldsymbol{\Psi}, \big(f^{(0)} + \xi f^{(1)}\big)\big\rangle = 0, \tag{2.23}$$

we obtain the Navier–Stokes equations

$$\frac{\partial \boldsymbol{Q}}{\partial t} + \frac{\partial \boldsymbol{G}^i}{\partial x} + \frac{\partial \boldsymbol{G}^v}{\partial x} = 0, \tag{2.24}$$

where the viscous flux vector

$$\boldsymbol{G}^v = -\frac{1}{\nu}\begin{pmatrix} 0 \\ (3-\gamma)\dfrac{\rho}{2\beta}\dfrac{\partial u_x}{\partial x} \\ (3-\gamma)\dfrac{\rho u_x}{2\beta}\dfrac{\partial u_x}{\partial x} - \dfrac{\gamma}{(\gamma-1)}\dfrac{\rho}{4\beta^3}\dfrac{\partial \beta}{\partial x} \end{pmatrix} = \begin{pmatrix} 0 \\ -\tau_{xx}^v \\ -u_x \tau_{xx}^v + \dot{q}_x^v \end{pmatrix}. \tag{2.25}$$

From the first-order viscous flux vector, we identify the molecular viscosity $\mu = p/\nu$ and thermal conductivity $\kappa = (\mu \gamma R)/(\gamma - 1)$ to obtain the familiar expressions for the

https://doi.org/10.1017/S0022112004007876 Published online by Cambridge University Press

Navier–Stokes (first-order) stress and heat flux

$$\tau_{xx}^{v} = (3-\gamma)\mu\frac{\partial u_x}{\partial x}, \quad \dot{q}_x^{v} = -\kappa\frac{\partial T}{\partial x} \tag{2.26}$$

and note that the Prandtl number $Pr = \mu C_p/\kappa = 1$, where C_p is the specific heat at constant pressure.

2.3. *Second-order distribution function: Model 1*

The second-order distribution function is defined by the first three terms of the Chapman–Enskog expansion

$$f = f^{(0)} + \xi f^{(1)} + \xi^2 f^{(2)}. \tag{2.27}$$

From (2.18), we obtain an expression for $f^{(2)}$ in terms of $f^{(1)}$

$$f^{(2)} = -\frac{1}{\xi\nu}\left[\frac{\partial}{\partial t}\left(f^{(1)}\right) + \frac{\partial}{\partial x}\left(u_x f^{(1)}\right) + \frac{\partial}{\partial x}\left(C_x f^{(0)}\phi^{(1)}\right)\right]. \tag{2.28}$$

Unlike the expression for $f^{(1)}$, it can be seen that (2.28) does not satisfy (2.22). This is not surprising, as the moment $\langle C_x\boldsymbol{\Psi}, f^{(0)}\phi^{(1)}\rangle$ gives rise to the viscous flux vector $\boldsymbol{G}^{v}$ in the Navier–Stokes equations. This calls for additional moment closure terms and associated coefficients that satisfy (2.22). From (2.28) and (2.21) we write

$$\left\langle C_x\boldsymbol{\Psi}, f^{(0)}\phi^{(1)}\right\rangle = \left\langle \boldsymbol{\Psi}, f^{(0)}\phi'^{(1)}\right\rangle. \tag{2.29}$$

where

$$\left.\begin{aligned}
\phi'^{(1)} &= C_x\phi^{(1)} \\
&= -\frac{1}{\xi\nu}\left[\mathscr{B}^{(1)}(I, C_x)\frac{\partial\beta}{\partial x} + \mathscr{B}^{(2)}(I, C_x)\frac{\partial u_x}{\partial x}\right], \\
\mathscr{B}^{(1)}(I, C_x) &= \frac{5}{2\beta}C_x^2 - \frac{I}{\beta I_0}C_x^2 - C_x^4, \\
\mathscr{B}^{(2)}(I, C_x) &= (3-\gamma)\beta C_x^3 - (\gamma-1)\frac{I}{I_0}C_x + \tfrac{1}{2}(3\gamma-5)C_x.
\end{aligned}\right\} \tag{2.30}$$

On evaluating the moments of $\mathscr{B}^{(1)}(I, C_x)$ in (2.30), we obtain

$$\left.\begin{aligned}
&\left\langle \boldsymbol{\Psi}_1 = 1, f^{(0)}\mathscr{B}^{(1)}(I, C_x)\right\rangle = 0, \\
&\left\langle \boldsymbol{\Psi}_2 = v_x, f^{(0)}\mathscr{B}^{(1)}(I, C_x)\right\rangle = 0, \\
&\left\langle \boldsymbol{\Psi}_3 = I + \tfrac{1}{2}v_x^2, f^{(0)}\mathscr{B}^{(1)}(I, C_x)\right\rangle = -\frac{\gamma\rho}{4\beta^3(\gamma-1)}.
\end{aligned}\right\} \tag{2.31}$$

Since the moment $\langle\boldsymbol{\Psi}, f^{(0)}\mathscr{B}^{(1)}(I, C_x)\rangle$ is not equal to zero, we need to include additional terms that are suitably weighted. It is evident that there is no unique expression for these additional terms. In an effort to keep the expression simple, we define a moment closure function

$$\widetilde{\mathscr{B}}^{(1)}(I, C_x) = \mathscr{B}^{(1)}(I, C_x) + \omega_1\left(\tfrac{1}{2}C_x^2 - C_x^4\right) + \omega_2\frac{I}{\beta I_0}C_x^2, \tag{2.32}$$

where the forms of the additional terms are chosen to be similar to those in $\mathscr{B}^{(1)}(I, C_x)$. We choose only two undetermined coefficients as there are only two

https://doi.org/10.1017/S0022112004007876 Published online by Cambridge University Press

equations available to complete the definition of $\widetilde{\mathscr{B}}^{(1)}(I, C_x)$

$$\left.\begin{aligned}&\left\langle I + \frac{C_x^2}{2},\, f^{(0)}\widetilde{\mathscr{B}}^{(1)}(I, C_x)\right\rangle = 0,\\ &\left\langle 1,\, f^{(0)}\widetilde{\mathscr{B}}^{(1)}(I, C_x)\right\rangle = 0.\end{aligned}\right\} \tag{2.33}$$

Calculating the moments in (2.33) yields the equations

$$\left\langle 1,\, f^{(0)}\widetilde{\mathscr{B}}^{(1)}(I, C_x)\right\rangle = 0 \Longleftrightarrow \omega_1 = 2\omega_2, \tag{2.34}$$

$$\left\langle I + \tfrac{1}{2}C_x^2,\, f^{(0)}\widetilde{\mathscr{B}}^{(1)}(I, C_x)\right\rangle = 0 \Longleftrightarrow \omega_2(\gamma + 3) - \omega_1(4\gamma - 3) = 2\gamma, \tag{2.35}$$

which give

$$\omega_1 = \left(\frac{4\gamma}{9 - 7\gamma}\right), \quad \omega_2 = \left(\frac{2\gamma}{9 - 7\gamma}\right). \tag{2.36}$$

Equation (2.32) is now written as

$$\widetilde{\mathscr{B}}^{(1)}(I, C_x) = \left(\frac{5}{2\beta} + \frac{\omega_1}{\beta}\right) C_x^2 + \frac{I}{\beta I_0} C_x^2 (\omega_2 - 1) - C_x^4 (1 + \omega_1). \tag{2.37}$$

The moments of $\widetilde{\mathscr{B}}^{(2)}(I, C_x)$ in (2.30) are evaluated in a similar manner. Since $\widetilde{\mathscr{B}}^{(2)}(I, C_x)$ is an odd function of C_x, all odd integrals over $\mathbb{R}$ disappear, yielding

$$\left.\begin{aligned}&\left\langle \boldsymbol{\Psi}_1 = 1,\, f^{(0)}\mathscr{B}^{(2)}(I, C_x)\right\rangle = 0,\\ &\left\langle \boldsymbol{\Psi}_2 = v_x,\, f^{(0)}\mathscr{B}^{(2)}(I, C_x)\right\rangle = (3 - \gamma)\frac{\rho}{2\beta},\\ &\left\langle \boldsymbol{\Psi}_3 = I + \tfrac{1}{2}v_x^2,\, f^{(0)}\mathscr{B}^{(2)}(I, C_x)\right\rangle = (3 - \gamma)\frac{\rho u_x}{2\beta}.\end{aligned}\right\} \tag{2.38}$$

As the moments with $\boldsymbol{\Psi}_2$ and $\boldsymbol{\Psi}_3$ in (2.38) are multiples of each other, we require only one undetermined coefficient in the moment closure function

$$\widetilde{\mathscr{B}}^{(2)}(I, C_x) = \mathscr{B}^{(2)}(I, C_x) + \omega_3 \left[\beta C_x^3 - \frac{I}{I_0} C_x + C_x\right]. \tag{2.39}$$

Evaluating the moment $\langle C_x,\, f^{(0)}\widetilde{\mathscr{B}}^{(2)}(I, C_x)\rangle$ and setting it equal to zero gives

$$\widetilde{\mathscr{B}}^{(2)}(I, C_x) = \beta((3 - \gamma) + \omega_3)C_x^3 - \frac{I}{I_0}((\gamma - 1) + \omega_3)C_x + \tfrac{1}{2}(3\gamma - 5) + \omega_3 C_x, \tag{2.40}$$

where

$$\omega_3 = -\tfrac{2}{3}(3 - \gamma). \tag{2.41}$$

The complete expression for the second-order distribution function is given by

$$f = f^{(0)} + \xi f^{(1)} - \frac{\xi}{\nu}\left[\frac{\partial}{\partial t}\left(f^{(1)}\right) + \frac{\partial}{\partial x}\left(u_x f^{(1)}\right) + \frac{\partial}{\partial x}\left(f^{(0)}\widetilde{\phi}^{(1)}\right)\right], \tag{2.42}$$

where

$$\left.\begin{aligned}\widetilde{\phi}^{(1)} &= -\frac{1}{\xi\nu}\left[\widetilde{\mathscr{B}}^{(1)}(I, C_x)\frac{\partial\beta}{\partial x} + \widetilde{\mathscr{B}}^{(2)}(I, C_x)\frac{\partial u_x}{\partial x}\right],\\ \widetilde{\mathscr{B}}^{(1)}(I, C_x) &= \frac{\theta_1}{\beta}C_x^2 + \theta_2\frac{I}{\beta I_0}C_x^2 + \theta_3 C_x^4,\\ \widetilde{\mathscr{B}}^{(2)}(I, C_x) &= \theta_4\beta C_x^3 + \theta_5\frac{I}{I_0}C_x + \theta_6 C_x,\end{aligned}\right\} \tag{2.43}$$

and the moment closure coefficients are given in table 1.

https://doi.org/10.1017/S0022112004007876 Published online by Cambridge University Press

$\omega_1 = \dfrac{4\gamma}{(9-7\gamma)}$	$\omega_2 = \dfrac{2\gamma}{(9-7\gamma)}$	$\omega_3 = -\frac{2}{3}(3-\gamma)$
$\theta_1 = \frac{5}{2} + \omega_1$	$\theta_2 = \omega_2 - 1$	$\theta_3 = -(1+\omega_1)$
$\theta_4 = (3-\gamma) + \omega_3$	$\theta_5 = -(\gamma-1) - \omega_3$	$\theta_6 = \frac{1}{2}(3\gamma-5) + \omega_3$

TABLE 1. Closure coefficients of the Model 1 second-order distribution function given by equations (2.42) and (2.43). These coefficients are functions of the specific heat ratio γ.

2.4. *BGK-Burnett equations: Model 1*

On taking moments of the Boltzmann equation for the second-order distribution function

$$\frac{\partial}{\partial t}\left\langle \boldsymbol{\Psi},\, f^{(0)} + \xi f^{(1)} + \xi^2 f^{(2)} \right\rangle + \frac{\partial}{\partial x}\left\langle v_x \boldsymbol{\Psi},\, f^{(0)} + \xi f^{(1)} + \xi^2 f^{(2)} \right\rangle = 0, \tag{2.44}$$

we obtain the BGK-Burnett equations

$$\frac{\partial \boldsymbol{Q}}{\partial t} + \frac{\partial \boldsymbol{G}^i}{\partial x} + \frac{\partial \boldsymbol{G}^v}{\partial x} + \frac{\partial \boldsymbol{G}^B}{\partial x} = 0. \tag{2.45}$$

The BGK-Burnett flux vector (second-order flux vector) is given by

$$\boldsymbol{G}^{\mathrm{B}} = \left\langle v_x \boldsymbol{\Psi}, -\frac{\xi}{\nu}\left[\frac{\mathscr{D}}{\mathscr{D}t} f^{(1)} + f^{(1)}\frac{\partial u_x}{\partial x} + \frac{\partial}{\partial x} f^{(0)} \widetilde{\phi}^{(1)}\right]\right\rangle = \begin{pmatrix} 0 \\ -\tau_{xx}^B \\ -u_x \tau_{xx}^B + \dot{q}_x^B \end{pmatrix}, \tag{2.46}$$

where $\mathscr{D}/\mathscr{D}t = \partial/\partial t + u_i \partial/\partial x_i$ is the material derivative operator. The BGK-Burnett stress and heat flux, τ_{xx}^B and $\dot{q}_x^B$, are given by

$$\begin{aligned}\tau_{xx}^B = -\frac{1}{\nu^2}\Bigg[&\frac{\Omega_1}{\beta}\frac{\mathscr{D}\rho}{\mathscr{D}t}\frac{\partial u_x}{\partial x} + \Omega_1\frac{\rho}{\beta}\frac{\mathscr{D}}{\mathscr{D}t}\left(\frac{\partial u_x}{\partial x}\right) - \Omega_1\frac{\rho}{\beta^2}\frac{\mathscr{D}\beta}{\mathscr{D}t}\frac{\partial u_x}{\partial x} + \Omega_1\frac{\rho}{\beta}\left(\frac{\partial u_x}{\partial x}\right)^2 + \frac{\Omega_2}{\beta^3}\frac{\partial \rho}{\partial x}\frac{\partial \beta}{\partial x} \\ &+ \Omega_2\frac{\rho}{\beta^3}\frac{\partial^2 \beta}{\partial x^2} - 3\Omega_2\frac{\rho}{\beta^4}\left(\frac{\partial \beta}{\partial x}\right)^2\Bigg] + \frac{1}{\nu^3}\left[\Omega_1\frac{\rho}{\beta}\frac{\partial u_x}{\partial x}\frac{\mathscr{D}\nu}{\mathscr{D}t} + \Omega_2\frac{\rho}{\beta^3}\frac{\partial \beta}{\partial x}\frac{\partial \nu}{\partial x}\right]\end{aligned} \tag{2.47}$$

and

$$\begin{aligned}\dot{q}_x^B = \frac{1}{\nu^2}\Bigg[&\Omega_1\frac{\rho}{\beta}\frac{\mathscr{D}u_x}{\mathscr{D}t}\frac{\partial u_x}{\partial x} - \frac{\Omega_3}{\beta^3}\frac{\mathscr{D}\rho}{\mathscr{D}t}\frac{\partial \beta}{\partial x} + 3\Omega_3\frac{\rho}{\beta^4}\frac{\mathscr{D}\beta}{\mathscr{D}t}\frac{\partial \beta}{\partial x} - \Omega_3\frac{\rho}{\beta^3}\frac{\mathscr{D}}{\mathscr{D}t}\left(\frac{\partial \beta}{\partial x}\right) \\ &+ (\Omega_2 - \Omega_3)\frac{\rho}{\beta^3}\frac{\partial \beta}{\partial x}\frac{\partial u_x}{\partial x} + \frac{\Omega_4}{\beta^2}\frac{\partial \rho}{\partial x}\frac{\partial u_x}{\partial x} + \Omega_4\frac{\rho}{\beta^2}\frac{\partial^2 u_x}{\partial x^2} - 2\Omega_4\frac{\rho}{\beta^3}\frac{\partial \beta}{\partial x}\frac{\partial u_x}{\partial x}\Bigg] \\ &+ \frac{1}{\nu^3}\left[\Omega_3\frac{\rho}{\beta^3}\frac{\partial \beta}{\partial x}\frac{\mathscr{D}\nu}{\mathscr{D}t} - \Omega_4\frac{\rho}{\beta^2}\frac{\partial u_x}{\partial x}\frac{\partial \nu}{\partial x}\right],\end{aligned} \tag{2.48}$$

where the second-order stress and heat flux coefficients are given in table 2. The presence of the material derivatives in (2.47) and (2.48) make the expressions for the BGK-Burnett stress and heat flux very general and give rise to a large number of representational forms. The various forms, which arise from the approximations employed in representing the material derivatives, and the choice of either considering the effects of spatio-temporal variations in the molecular collision frequency or not, open up the potential to formulate expressions for τ_{xx}^B and $\dot{q}_x^B$ that make the BGK-Burnett equations entropy-consistent.

https://doi.org/10.1017/S0022112004007876 Published online by Cambridge University Press

$$\Omega_1 = \tfrac{1}{2}(3-\gamma) \qquad \Omega_2 = \tfrac{3}{4}\left(\theta_1 + \theta_2 + \tfrac{5}{2}\theta_3\right)$$
$$\Omega_3 = \frac{\gamma}{4(\gamma-1)} \qquad \Omega_4 = \frac{1}{8(\gamma-1)}[\theta_4(6\gamma-3) + \theta_5(\gamma+3) + \theta_6(2\gamma)]$$

TABLE 2. Stress and heat flux coefficients of the Model 1 equations (2.47) and (2.48). These coefficients are functions of the Model 1 closure coefficients and the specific heat ratio γ.

2.4.1. *Model 1a: second-order flux without the derivatives $\mathscr{D}v/\mathscr{D}t$ and $\partial v/\partial x$*

In this model of the second-order stress and heat flux, the derivatives $\mathscr{D}v/\mathscr{D}t$ and $\partial v/\partial x$ in equations (2.47) and (2.48) are neglected. This assumption is based on the observation that, in weak shocks, the rise in the pressure p and molecular viscosity μ is such that the variations in the ratio $v = p/\mu$ could be neglected (see figures 7*a* and 7*b* and the explanation in §4 for the rationale behind this assumption). The expressions for the Model 1a stress and heat flux take the form

$$\tau^B_{xx} = -\frac{\mu^2}{p}\left[2\Omega_1 \underbrace{\left(\frac{1}{\rho}\frac{\mathscr{D}\rho}{\mathscr{D}t} + \frac{1}{T}\frac{\mathscr{D}T}{\mathscr{D}t}\right)}_{1a}\frac{\partial u_x}{\partial x} + 2\Omega_1\frac{\mathscr{D}}{\mathscr{D}t}\left(\frac{\partial u_x}{\partial x}\right) + 2\Omega_1\left(\frac{\partial u_x}{\partial x}\right)^2 - 4\Omega_2 R\frac{\partial^2 T}{\partial x^2} - 4\Omega_2 R\underbrace{\left(\frac{1}{\rho}\frac{\partial\rho}{\partial x} + \frac{1}{T}\frac{\partial T}{\partial x}\right)}_{2a}\frac{\partial T}{\partial x}\right] \quad (2.49)$$

and

$$\dot{q}^B_x = \frac{\mu^2}{\rho}\left[\frac{4\Omega_3}{T}\underbrace{\left(\frac{1}{\rho}\frac{\mathscr{D}\rho}{\mathscr{D}t} + \frac{1}{T}\frac{\mathscr{D}T}{\mathscr{D}t}\right)}_{3a}\frac{\partial T}{\partial x} + 4\Omega_4\underbrace{\left(\frac{1}{\rho}\frac{\partial\rho}{\partial x} + \frac{1}{T}\frac{\partial T}{\partial x}\right)}_{4a}\frac{\partial u_x}{\partial x} + 4\Omega_4\frac{\partial^2 u_x}{\partial x^2} + \frac{4\Omega_3}{T}\frac{\mathscr{D}}{\mathscr{D}t}\left(\frac{\partial T}{\partial x}\right) + 4(\Omega_4 - \Omega_2 + \Omega_3)\frac{1}{T}\frac{\partial T}{\partial x}\frac{\partial u_x}{\partial x} + \frac{2\Omega_1}{RT}\frac{\mathscr{D}u_x}{\mathscr{D}t}\frac{\partial u_x}{\partial x}\right]. \quad (2.50)$$

On using the continuity equation to express $\mathscr{D}\rho/\mathscr{D}t$ and the Euler equations to express the material derivatives $\mathscr{D}u_x/\mathscr{D}t$ and $\mathscr{D}T/\mathscr{D}t$ in (2.49) and (2.50), we obtain

$$\tau^B_{xx} = -\frac{\mu^2}{p}\left[-2\Omega_1\left(\frac{\partial u_x}{\partial x}\right)^2 + 2\Omega_1\frac{\mathscr{D}}{\mathscr{D}t}\left(\frac{\partial u_x}{\partial x}\right) - 4\Omega_2\frac{R}{\rho}\frac{\partial\rho}{\partial x}\frac{\partial T}{\partial x} - 4\Omega_2 R\frac{\partial^2 T}{\partial x^2} - 4\Omega_2\frac{R}{T}\left(\frac{\partial T}{\partial x}\right)^2\right] \quad (2.51)$$

and

$$\dot{q}^B_x = \frac{\mu^2}{\rho}\left[(8\Omega_4 - 4\Omega_2 - 4\Omega_3(\gamma-1) - 2\Omega_1)\frac{1}{T}\frac{\partial T}{\partial x}\frac{\partial u_x}{\partial x} + 4\Omega_3\frac{1}{T}\frac{\mathscr{D}}{\mathscr{D}t}\left(\frac{\partial T}{\partial x}\right) + 4\Omega_4\left(\frac{\partial^2 u_x}{\partial x^2}\right) + (4\Omega_4 - 2\Omega_1)\frac{1}{\rho}\frac{\partial\rho}{\partial x}\frac{\partial u_x}{\partial x}\right]. \quad (2.52)$$

https://doi.org/10.1017/S0022112004007876 Published online by Cambridge University Press

2.4.2. *Model 1b: second-order flux with derivatives $\mathscr{D}\nu/\mathscr{D}t$ and $\partial\nu/\partial x$ present*

In this model, we retain the material and spatial derivatives of the collision frequency $\mathscr{D}\nu/\mathscr{D}t$ and $\partial\nu/\partial x$, respectively. Substituting $\nu = p/\mu$ in equations (2.47) and (2.48), and using the continuity and Euler equations to express the material derivatives $\mathscr{D}\rho/\mathscr{D}t$, $\mathscr{D}u_x/\mathscr{D}t$ and $\mathscr{D}T/\mathscr{D}t$ gives

$$\tau_{xx}^B = -\frac{\mu^2}{p}\left[2\Omega_1 \underbrace{\left(\frac{1}{\mu}\frac{\mathscr{D}\mu}{\mathscr{D}t}\right)}_{1b}\frac{\partial u_x}{\partial x} + 2\Omega_1\frac{\mathscr{D}}{\mathscr{D}t}\left(\frac{\partial u_x}{\partial x}\right) + 2\Omega_1\left(\frac{\partial u_x}{\partial x}\right)^2 - 4\Omega_2 R\frac{\partial^2 T}{\partial x^2} - 4\Omega_2 R\underbrace{\left(\frac{1}{\mu}\frac{\partial\mu}{\partial x}\right)}_{2b}\frac{\partial T}{\partial x}\right] \quad (2.53)$$

and

$$\dot{q}_x^B = \frac{\mu^2}{\rho}\left[\frac{4\Omega_3}{T}\underbrace{\left(\frac{1}{\mu}\frac{\mathscr{D}\mu}{\mathscr{D}t}\right)}_{3b}\frac{\partial T}{\partial x} + 4\Omega_4\underbrace{\left(\frac{1}{\mu}\frac{\partial\mu}{\partial x}\right)}_{4b}\frac{\partial u_x}{\partial x} + 4\Omega_4\frac{\partial^2 u_x}{\partial x^2} + \frac{4\Omega_3}{T}\frac{\mathscr{D}}{\mathscr{D}t}\left(\frac{\partial T}{\partial x}\right) + 4(\Omega_4 - \Omega_2 + \Omega_3)\frac{1}{T}\frac{\partial T}{\partial x}\frac{\partial u_x}{\partial x} + \frac{2\Omega_1}{RT}\frac{\mathscr{D}u_x}{\mathscr{D}t}\frac{\partial u_x}{\partial x}\right]. \quad (2.54)$$

When the force of repulsion between gas molecules is modelled as $F \propto 1/r^n$, where r is the distance between molecules, it can be shown from kinetic theory that the variation of viscosity with temperature is given by the power law constitutive relation

$$\mu/\mu_{ref} = (T/T_{ref})^{\omega}, \quad (2.55)$$

where the exponent $\omega = 1/2 + 2/(n-1)$. Since the formulation of the BGK-Burnett equations assumes the gas molecules to be rigid elastic spheres, the so-called hard sphere gas, we set $n = \infty$ to obtain $\omega = 0.5$. By using (2.55) to express the material and spatial derivatives $\mathscr{D}\mu/\mathscr{D}t$ and $\partial\mu/\partial x$ in equations (2.53) and (2.54), we obtain

$$\tau_{xx}^B = -\frac{\mu^2}{p}\left[2\Omega_1(1-\omega(\gamma-1))\left(\frac{\partial u_x}{\partial x}\right)^2 + 2\Omega_1\frac{\mathscr{D}}{\mathscr{D}t}\left(\frac{\partial u_x}{\partial x}\right) - 4\Omega_2 R\frac{\partial^2 T}{\partial x^2} - 4\Omega_2\frac{\omega R}{T}\left(\frac{\partial T}{\partial x}\right)^2\right] \quad (2.56)$$

and

$$\dot{q}_x^B = \frac{\mu^2}{\rho}\left[(4\Omega_4 - 4\Omega_2 + 4\Omega_3(1-\omega(\gamma-1)) + 4\Omega_4\omega - 2\Omega_1)\frac{1}{T}\frac{\partial T}{\partial x}\frac{\partial u_x}{\partial x} + 4\Omega_3\frac{1}{T}\frac{\mathscr{D}}{\mathscr{D}t}\left(\frac{\partial T}{\partial x}\right) + 4\Omega_4\frac{\partial^2 u_x}{\partial x^2} - 2\Omega_1\frac{1}{\rho}\frac{\partial\rho}{\partial x}\frac{\partial u_x}{\partial x}\right]. \quad (2.57)$$

2.4.3. *Comparing the Model 1a, Model 1b, Burnett and Woods second-order flux*

On comparing the stress in Model 1a (2.51) with the stress in the Burnett equation (2.58) (see Welder *et al.* 1993) we notice that both sets of expressions have the same set of derivatives, although the coefficients are different. In the Model 1b stress (2.56),

https://doi.org/10.1017/S0022112004007876 Published online by Cambridge University Press

$\omega_1 = \frac{4}{3}\left(\frac{7}{2} - \omega\right)$	$\omega_2 = 2$	$\omega_3 = 3$
$\omega_4 = 0$	$\omega_5 = 3\omega$	$\omega_6 = 8$
$\theta_1 = \frac{15}{4}\left(\frac{7}{2} - \omega\right)$	$\theta_2 = \frac{45}{8}$	$\theta_3 = -3$
$\theta_4 = 3$	$\theta_5 = 3\left(\frac{35}{4} + \omega\right)$	

TABLE 3. Burnett stress and heat flux coefficients in equations (2.58) and (2.59) from Welder *et al.* (1993). These coefficients must not be confused with the Model 1 closure coefficients (see table 1). These coefficients are functions of the exponent ω in the viscosity relation $\mu/\mu_{ref} = \left(T/T_{ref}\right)^{\omega}$.

$\tilde{\omega}_1 = \frac{4}{3}(4 - \omega)$	$\tilde{\omega}_3 = 3$	$\tilde{\omega}_5 = 3\omega$	$\tilde{\omega}_6 = 6$
$\tilde{\theta}_1 = \frac{15}{4}\left(\frac{9}{2} - \omega\right)$	$\tilde{\theta}_2 = \frac{45}{4}$	$\tilde{\theta}_5 = 3\left(\frac{35}{4} + \omega\right)$	

TABLE 4. Woods stress and heat flux coefficients in equations (2.60) and (2.61) from Reese *et al.* (1995).These coefficients, like the Burnett coefficients are functions of the exponent ω in the viscosity relation $\mu/\mu_{ref} = (T/T_{ref})^{\omega}$.

we note the absence of the term $(R/\rho)(\partial\rho/\partial x)(\partial T/\partial x)$ which is present in (2.51) and (2.58). A comparison of the Model 1b stress with the Woods stress (see Reese *et al.* 1995) reveals that the material derivative $\mathscr{D}/\mathscr{D}t(\partial u_x/\partial x)$ that is present in (2.56) is absent in (2.60). A comparison of the heat flux in Model 1a (2.52) and Model 1b (2.57) shows that including the material and spatial derivatives of the collision frequency do not affect the derivatives present in the heat flux. Further, both these heat flux expressions have the same derivatives that are present in the Burnett heat flux (2.59). The expression for the Woods heat flux (2.61) does not have the terms $(1/\rho)(\partial\rho/\partial x)(\partial u_x/\partial x)$ and $\partial^2 u_x/\partial x^2$ that are present in (2.52), (2.57) and (2.59).

$$\tau_{xx}^{oB} = -\frac{\mu^2}{p}\left[\left(\tfrac{2}{3}\omega_1 - \tfrac{8}{9}\omega_2 + \tfrac{2}{9}\omega_6\right)\left(\frac{\partial u_x}{\partial x}\right)^2 + \tfrac{2}{3}\omega_2\frac{\mathscr{D}}{\mathscr{D}t}\left(\frac{\partial u_x}{\partial x}\right) + \tfrac{2}{3}\omega_4\frac{R}{\rho}\frac{\partial\rho}{\partial x}\frac{\partial T}{\partial x} + \tfrac{2}{3}\omega_3 R\frac{\partial^2 T}{\partial x^2} + \tfrac{2}{3}(\omega_4 + \omega_5)\frac{R}{T}\left(\frac{\partial T}{\partial x}\right)^2\right], \quad (2.58)$$

$$\dot{q}_x^{oB} = \frac{\mu^2}{\rho}\left[\left(\theta_1 - \theta_2 + \tfrac{2}{3}\theta_3 + \tfrac{2}{3}\theta_5\right)\frac{1}{T}\frac{\partial u_x}{\partial x}\frac{\partial T}{\partial x} + \theta_2\frac{1}{T}\frac{\mathscr{D}}{\mathscr{D}t}\left(\frac{\partial T}{\partial x}\right) + \tfrac{2}{3}\theta_4\frac{\partial^2 u_x}{\partial x^2} + \tfrac{2}{3}\theta_3\frac{1}{\rho}\frac{\partial\rho}{\partial x}\frac{\partial u_x}{\partial x}\right], \quad (2.59)$$

$$\tau_{xx}^{W} = -\frac{\mu^2}{p}\left[\left(\tfrac{2}{3}\tilde{\omega}_1 + \tfrac{2}{9}\tilde{\omega}_6\right)\left(\frac{\partial u_x}{\partial x}\right)^2 + \tfrac{2}{3}\tilde{\omega}_3 R\frac{\partial^2 T}{\partial x^2} + \tfrac{2}{3}\tilde{\omega}_5\frac{R}{T}\left(\frac{\partial T}{\partial x}\right)^2\right], \quad (2.60)$$

$$\dot{q}_x^{W} = \frac{\mu^2}{\rho}\left[\left(\tilde{\theta}_1 + \tfrac{2}{3}\tilde{\theta}_5\right)\frac{1}{T}\frac{\partial u_x}{\partial x}\frac{\partial T}{\partial x} + \tilde{\theta}_2\frac{1}{T}\frac{\mathscr{D}}{\mathscr{D}t}\left(\frac{\partial T}{\partial x}\right)\right]. \quad (2.61)$$

The expressions for the stress and heat flux coefficients in the Burnett and Woods equations are given in tables 3 and 4. It must be noted, that although the derivatives in the stress expressions in equations (2.51) and (2.58) are the same, the coefficients are quite different. The same is true of the heat flux equations (2.52), (2.57) and (2.59). While the stress and heat flux coefficients in the Burnett and Woods equations are functions of the exponent ω in equation (2.53), the stress and heat flux coefficients

https://doi.org/10.1017/S0022112004007876 Published online by Cambridge University Press

$\tau_{xx}^{(II)}$ and $\dot{q}_x^{(II)}$	BGK-Burnett Model 1a	Burnett	BGK-Burnett Model 1b	Woods
A_1	**−1.3333**	2.6667	0.889	4.444
A_2	1.3333	1.3333	1.3333	0
A_3	**−4.5**	0.0	0.0	0.0
A_4	**−4.5**	2.0	**−4.5**	2.0
A_5	**−4.5**	1.0	**−2.25**	1.0
B_1	**−5.722**	22.125	**−2.833**	33.5
B_2	2.5	5.625	2.5	11.25
B_3	0.889	2.0	0.889	0
B_4	−0.444	−2.0	−1.333	0

TABLE 5. A comparison of the Model 1a, Model 1b, Burnett and Woods stress and heat flux coefficients for a monatomic hard sphere gas, i.e. $\gamma = 1.666$, $\omega = 0.5$. Boldface characters highlight the Model 1a and Model 1b coefficients that have a different sign when compared with the Burnett and Woods coefficients.

of the BGK-Burnett equations are functions of the specific heat ratio γ. In order to compare the magnitudes of these coefficients, the second-order stress and heat flux are written in the generic form shown in equations (2.62) and (2.63) where the functional form of the coefficients $A_j \,\forall\, j = 1, \ldots, 5$ and $B_k \,\forall\, k = 1, \ldots, 4$ may be identified from the expressions for the stress and heat flux in the corresponding equations.

$$\tau_{xx}^{(II)} = -\frac{\mu^2}{p}\left[A_1\left(\frac{\partial u_x}{\partial x}\right)^2 + A_2\frac{\mathscr{D}}{\mathscr{D}t}\left(\frac{\partial u_x}{\partial x}\right) + A_3\frac{R}{\rho}\frac{\partial \rho}{\partial x}\frac{\partial T}{\partial x} + A_4 R\frac{\partial^2 T}{\partial x^2} + A_5\frac{R}{T}\left(\frac{\partial T}{\partial x}\right)^2\right], \tag{2.62}$$

$$\dot{q}_x^{(II)} = \frac{\mu^2}{\rho}\left[B_1\frac{1}{T}\frac{\partial u_x}{\partial x}\frac{\partial T}{\partial x} + B_2\frac{1}{T}\frac{\mathscr{D}}{\mathscr{D}t}\left(\frac{\partial T}{\partial x}\right) + B_3\frac{\partial^2 u_x}{\partial x^2} + B_4\frac{1}{\rho}\frac{\partial \rho}{\partial x}\frac{\partial u_x}{\partial x}\right]. \tag{2.63}$$

A comparison of the stress and heat flux coefficients of the Model 1a, Model 1b, Burnett and Woods equations for a monatomic hard sphere gas is presented in table 5. It is observed that inclusion of the material and spatial derivatives of the collision frequency changes the sign of the A_1 coefficient that multiplies the $(\partial u_x/\partial x)^2$ term in the Model 1a and Model 1b equations. Since the $(\partial u_x/\partial x)^2$ term assumes large values for strong shocks, the behaviour of the Model 1b equations, when applied to the shock structure problem, can be expected to be quite different from the Model 1a equations.

2.5. *An approach to identifying entropy consistent BGK-Burnett equations*

As mentioned earlier, the mere requirement that the moment closure equation be satisfied, gives rise to a family of BGK-Burnett equations where each set of BGK-Burnett equations is based on a set of non-unique closure coefficients and approximations to the material derivatives in the second-order stress and heat flux. Since there are a multitude of approximations for the material derivatives, each of which must, subsequently, be tested for entropy consistency, certain criteria must be imposed to identify a set of candidate approximations. The requirement that the linearized BGK-Burnett equations be stable to small perturbations, is one such criterion. The set of stable approximations to the material derivatives constitutes the short list of candidate approximations that is used in the complete set of nonlinear equations to solve for the shock structure in monatomic hard sphere gases. The task

https://doi.org/10.1017/S0022112004007876 Published online by Cambridge University Press

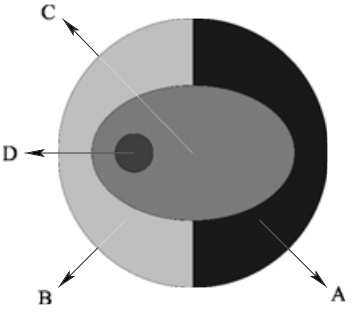


FIGURE 2. This diagram shows the approach taken to identify entropy-consistent BGK-Burnett equations. The region 'A' denotes the family of Model xa equations that are formed by neglecting the $\mathscr{D}v/\mathscr{D}t$ and $\partial v/\partial x$ in equations (2.47) and (2.48). The region 'B' denotes the family of Model xb equations that are formed by retaining the material and spatial derivatives of the collision frequency v. The linearized Model xa and Model xb equations are identical, the set of stable linearized equations obtained by considering various approximations to the material derivatives is denoted by the region 'C'. The material derivatives $\mathscr{D}/\mathscr{D}t(\partial u_x/\partial x)$ and $\mathscr{D}/\mathscr{D}t(\partial T/\partial x)$ in the stress and heat flux in each of these families (see equations (2.51), (2.52), (2.56), (2.57)) needs to be approximated since it is shown in § 3 that the exact form of the material derivatives do not make the equations stable and entropy-consistent. Since the Model xa equations are shown to be incorrect in § 4 (due to the fictitious viscosity $\tilde{\mu}$), we use the entropy-consistent relaxation technique, described in § 6, to identify those stable approximations to the material derivatives that will also make the Model xb equations entropy-consistent. The set of entropy-consistent Model xb equations is denoted by the region 'D'. Using this approach, it is shown in § 7 that the Model 2b equations are entropy-consistent.

of identifying an entropy-consistent set of BGK-Burnett equations is approached (see figure 2) by posing the following questions:

(i) Given a set of closure coefficients that satisfy the moment closure relationship, what approximations to the material derivatives will yield a stable set of linearized equations?

(ii) Given a set of approximations to the material derivatives that guarantees stability of the linearized BGK-Burnett equations, how do we identify a set of approximations that is also entropy-consistent?

The answer to the first question is obtained by linearizing the BGK-Burnett equations and looking for approximations to the material derivatives that make the linearized system stable. The answer to the second question lies in the entropy-consistent relaxation technique (ECRT) that is developed in §§ 6 and 7. For each set of closure coefficients that satisfy the moment closure criterion, the proposed methodology is a two-stage process that looks for stable approximations to the material derivative that are also entropy-consistent.

3. Linearized stability analysis of the BGK-Burnett equations

From table 5 we note that there are significant differences between the stress and heat flux coefficients of the Model 1a, Model 1b, Burnett and Woods stress and heat flux relations. A first step in the analysis of the Model 1 equations was a comparison of the stability characteristics of the Model 1, Burnett and Woods equations when subjected to small perturbations. In particular, the linearized stability analysis of the Model 1 equations was performed to identify approximations to the material derivatives $\mathscr{D}/\mathscr{D}t(\partial u_x/\partial x)$ and $\mathscr{D}/\mathscr{D}t(\partial T/\partial x)$ in the Model 1a and Model 1b stress and heat flux that would stabilize the equations. By linearizing the nonlinear Burnett

https://doi.org/10.1017/S0022112004007876 Published online by Cambridge University Press

equations and checking the resulting set of homogeneous equations for stability, it has been shown by Bobylev (1982) that the linearized Burnett equations are unstable when the local Knudsen number increases above a certain critical value. This technique was subsequently exploited by Zhong (1991) to develop a set of augmented Burnett equations which was shown to be stable for a wide range of local Knudsen numbers. The direct correlation between the unstable nature of the Burnett equations, as shown by the relatively simple linearized stability analysis of Bobylev, and the small wavelength instabilities experienced by Fiscko & Chapman (1988), indicated that stability of the linearized higher-order equations may be a necessary condition to ensure the stability of the second-order nonlinear hydrodynamic equations. In keeping with this line of thought, the stability aspects of the linearized BGK-Burnett Model 1 equations were investigated by examining the response of the linearized BGK-Burnett equations to a periodic perturbation wave (see Zhong 1991). On introducing the non-dimensional perturbation variables

$$\left.\begin{aligned} \rho' &= (\rho - \rho_\infty)/\rho_\infty, \\ u'_x &= (u_x - M_\infty\sqrt{\gamma RT_\infty})/\sqrt{RT_\infty}, \\ T' &= (T - T_\infty)/T_\infty, \end{aligned}\right\} \tag{3.1}$$

in the continuity, momentum and energy equations we obtain the linearized set of governing equations

$$\left.\begin{aligned} &\frac{\partial\rho'}{\partial t'} + M_\infty\sqrt{\gamma}\frac{\partial\rho'}{\partial x'} + \frac{\partial u'_x}{\partial x'} = 0, \\ &\frac{\partial u'_x}{\partial t'} + \frac{\partial\rho'}{\partial x'} + M_\infty\sqrt{\gamma}\frac{\partial u'_x}{\partial x'} + \frac{\partial T'}{\partial x'} = \frac{1}{p_\infty}\frac{\partial\tau_{xx}}{\partial x'}, \\ &\frac{\partial T'}{\partial t'} + (\gamma-1)\frac{\partial u'_x}{\partial x'} + M_\infty\sqrt{\gamma}\frac{\partial T'}{\partial x'} = -\frac{(\gamma-1)}{p_\infty\sqrt{RT_\infty}}\frac{\partial q'_x}{\partial x'}, \end{aligned}\right\} \tag{3.2}$$

where $x' = x/L_{ref}$ and $t' = t/t_{ref} = (p_\infty t)/\mu_\infty$ are the non-dimensional length and time scales, respectively. In arriving at the above set of equations it has been assumed that the perturbations are small. As a result, products and powers of the derivatives of flow variables are neglected. We study the response of equations (3.2) to a periodic perturbation wave given by

$$[\rho', u'_x, T']^T = [\epsilon_1, \epsilon_2, \epsilon_3]^T \mathrm{e}^{\mathrm{i}\omega x'}, \tag{3.3}$$

where ϵ_k satisfies the inequality $|\epsilon_k| \ll 1$, $\forall\, k = 1, 2, 3$. The characteristic length can also be written as $L_{ref} = \mu_\infty/\rho_\infty\sqrt{RT_\infty} = 0.783\lambda_\infty$ where λ_∞ denotes the free-stream mean free path. The non-dimensional circular frequency, $\omega = 2\pi L_{ref}/L = 4.92\lambda_\infty/L = 4.92Kn$. The linearized governing equations are written in vector-matrix form as

$$\frac{\partial \boldsymbol{V}'}{\partial t'} + \boldsymbol{M}_1\frac{\partial \boldsymbol{V}'}{\partial x'} = \begin{pmatrix} 0 \\ \dfrac{1}{p_\infty}\dfrac{\partial\tau_{xx}}{\partial x'} \\ -\dfrac{(\gamma-1)}{p_\infty\sqrt{RT_\infty}}\dfrac{\partial q'_x}{\partial x'} \end{pmatrix}, \tag{3.4}$$

where

$$\boldsymbol{V}' = [\rho', u'_x, T']^T \tag{3.5}$$

https://doi.org/10.1017/S0022112004007876 Published online by Cambridge University Press

$$\boldsymbol{M}_1 = \begin{pmatrix} M_\infty\sqrt{\gamma} & 1 & 0 \\ 1 & M_\infty\sqrt{\gamma} & 1 \\ 0 & (\gamma-1) & M_\infty\sqrt{\gamma} \end{pmatrix}. \tag{3.6}$$

Equation (3.4) forms the basis for the stability analysis of the various forms of the BGK-Burnett equations that arise from the different closure coefficients of the BGK-Burnett equations and the different approximations to the material derivatives in the BGK-Burnett stress and heat flux expressions. We assume the solution of equation (3.4) to be of the form

$$\boldsymbol{V}' = \bar{\boldsymbol{V}}\mathrm{e}^{\mathrm{i}\omega x'}\mathrm{e}^{\phi t'}, \tag{3.7}$$

where $\phi = \alpha + \mathrm{i}\beta$ and α and β denote the attenuation and dispersion coefficients, respectively. The initial conditions for equation (3.4) are given by the vector $\boldsymbol{V}'|_{t=0} = \bar{\boldsymbol{V}}\mathrm{e}^{\mathrm{i}\omega x'}$. For the system of equations to be stable we require $\alpha \leqslant 0$ as L decreases or, in other words, the disturbance must attenuate for increasing local Knudsen numbers.

3.1. *Characteristic polynomials and stability trajectories*

On substituting equation (3.7) and the Navier–Stokes expressions for the stress and heat flux in equation (3.4), we obtain the stability equation

$$\frac{\partial \boldsymbol{V}'}{\partial t'} + \boldsymbol{M}_1\frac{\partial \boldsymbol{V}'}{\partial x'} + \boldsymbol{M}_2\frac{\partial^2 \boldsymbol{V}'}{\partial x'^2} = 0, \tag{3.8}$$

where

$$\boldsymbol{M}_2 = \begin{pmatrix} 0 & 0 & 0 \\ 0 & -(3-\gamma) & 0 \\ 0 & 0 & -\dfrac{\gamma}{Pr} \end{pmatrix}. \tag{3.9}$$

Substituting equation (3.7) in equation (3.8) and imposing the requirement of non-trivial solutions, reduces the homogeneous equation (3.8) to an eigenvalue problem, where the condition

$$|\phi\boldsymbol{I} + \mathrm{i}\omega\boldsymbol{M}_1 - \omega^2\boldsymbol{M}_2| = 0 \tag{3.10}$$

must be satisfied. On expanding the determinant we obtain the characteristic polynomial whose roots are plotted on the complex plane for increasing local Knudsen numbers. For stability, the trajectory of the roots must lie on the left half of the complex plane. From the stability plot in figure 3(*a*), it is seen that the Navier–Stokes equations for a monatomic hard sphere gas are stable for increasing Knudsen numbers. It must be noted that the linearized forms of the Model 1a and Model 1b equations are the same; since the differences that arise by neglecting and retaining, respectively, the material and spatial derivatives of the collision frequency affect only the nonlinear terms. Consequently, the stability plots of the Model 1 equations are applicable for the Model 1a as well as Model 1b equations. However, on substituting the exact expression for the second-order stress and heat flux in equation (3.4) and plotting the roots of the characteristic polynomial, it can be seen from figure 3(*b*) that the exact Model 1 equations for a monatomic hard sphere gas are unstable. The term *exact*' means that the exact expressions for the material derivatives $\mathscr{D}/\mathscr{D}t(\partial u_x/\partial x) = \partial/\partial t(\partial u_x/\partial x) + u_x\partial^2 u_x/\partial x^2$ and $\mathscr{D}/\mathscr{D}t(\partial T/\partial x) = \partial/\partial t(\partial T/\partial x) + u_x\partial^2 T/\partial x^2$ were used in the second-order stress and heat flux. A similar instability is also observed with the exact Burnett and exact Woods equations (see Welder *et al.* 1993). This indicates the need for approximating the material derivatives $\mathscr{D}/\mathscr{D}t(\partial u_x/\partial x)$ and $\mathscr{D}/\mathscr{D}t(\partial T/\partial x)$ in the second-order fluxes.

https://doi.org/10.1017/S0022112004007876 Published online by Cambridge University Press

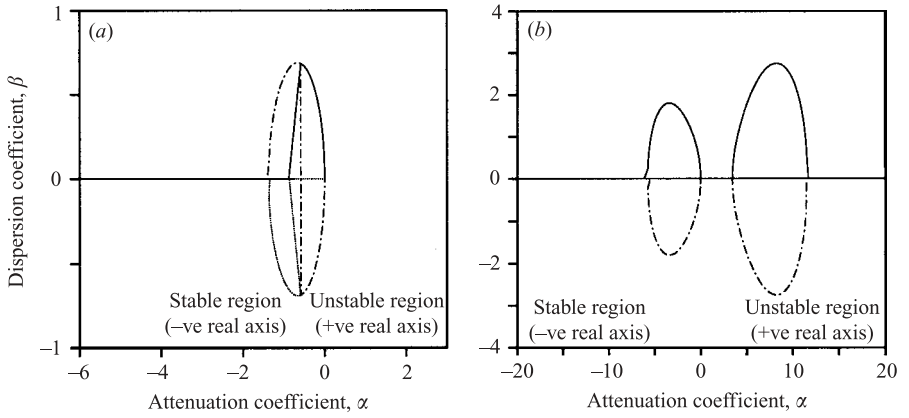


FIGURE 3. Stability plots of the linearized Navier–Stokes equations and exact BGK-Burnett Model 1 equations for a monatomic hard sphere gas. The term exact means that the material derivatives in the second-order fluxes were not approximated. While the Navier–Stokes equations (*a*) are stable for increasing Knudsen numbers, the exact BGK-Burnett Model 1 equations (*b*) are unstable. This indicates the need for approximating the material derivatives.

	Exact (no approx.) for $\mathscr{D}/\mathscr{D}t(\mathscr{A})$ $\mathscr{D}/\mathscr{D}t(\mathscr{B})$	Steady state for $\mathscr{D}/\mathscr{D}t(\mathscr{A})$ $\mathscr{D}/\mathscr{D}t(\mathscr{B})$	Euler based approx. for $\mathscr{D}/\mathscr{D}t(\mathscr{A})$ $\mathscr{D}/\mathscr{D}t(\mathscr{B})$	N–S based approx. for $\mathscr{D}/\mathscr{D}t(\mathscr{A})$ $\mathscr{D}/\mathscr{D}t(\mathscr{B})$	N–S based approx. for $\mathscr{D}/\mathscr{D}t(\mathscr{A})$ and $\mathscr{D}/\mathscr{D}t(\mathscr{B})=0$	N–S based approx. for $\mathscr{D}/\mathscr{D}t(\mathscr{B})$ and $\mathscr{D}/\mathscr{D}t(\mathscr{A})=0$
Model 1	Unstable	Unstable	Stable	Stable	Unstable	Unstable
Burnett	Unstable	Stable	Unstable	Stable	Unstable	Unstable
Woods	Unstable	Stable*	Unstable	Stable**	Stable*	Stable**

TABLE 6. A comparison of the stability characteristics of the linearized Model 1, Burnett and Woods equations for a monatomic hard sphere gas. In this table $\mathscr{A}=\partial u_x/\partial x$ and $\mathscr{B}=\partial T/\partial x$. The linearized Model 1 equations are stabilized by Euler and Navier–Stokes approximations to both the material derivatives, the Burnett equations are stabilized when steady state and Navier–Stokes approximations are used for both the material derivatives and the Woods equations are stabilized when the steady state and the Navier–Stokes approximations are used for the material derivative $\mathscr{D}/\mathscr{D}t(\mathscr{B})$. For the linearized Woods equations, the single * and double ** asterisk superscripts in columns 3 and 6, and columns 5 and 7, respectively, indicate that the results of the stability analysis in these columns are the same.

Since the second-order stress and heat flux vary on a faster time scale than the conserved quantities in the state vector $\boldsymbol{Q}$, it seemed reasonable to assume that they would have steady-state values on the time scales on which the conserved variables are evolved. Consequently, the material derivatives were approximated by the steady-state approximations, i.e. $\mathscr{D}/\mathscr{D}t(\partial u_x/\partial x)\approx u_x\partial^2 u_x/\partial x^2$ and $\mathscr{D}/\mathscr{D}t(\partial T/\partial x)\approx u_x\partial^2 T/\partial x^2$. It was noticed, as shown in table 6, that this approximation stabilizes (see Welder *et al.* 1993) the linearized Burnett and Woods equations but did not stabilize the linearized Model 1 equations. Various other approximations to the material derivatives were considered, as shown in table 6, and it is observed that the only approximations that make the linearized Model 1 equations stable (see figure 4) are the Euler and Navier–Stokes approximations to the material derivatives. When both the material derivatives are neglected, it is seen that the linearized Model 1 equations are unstable while the linearized Burnett and Woods equations are stable. This is not surprising

https://doi.org/10.1017/S0022112004007876 Published online by Cambridge University Press

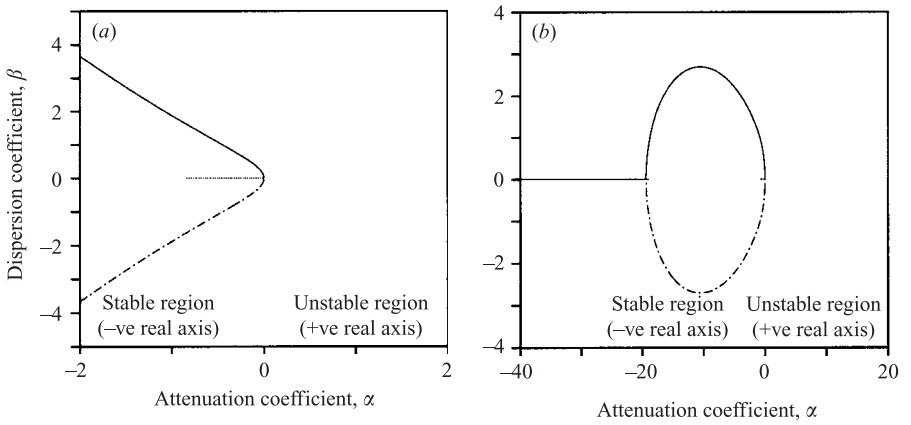


FIGURE 4. Stability plots of the BGK-Burnett Model 1 equations for a monatomic hard sphere gas with (*a*) Euler and (*b*) Navier–Stokes approximations for the material derivatives $\mathscr{D}/\mathscr{D}t(\partial u_x/\partial x)$ and $\mathscr{D}/\mathscr{D}t(\partial T/\partial x)$. It can be seen that the Model 1 equations are stable with these approximations to both the material derivatives.

as it is a special case of the steady-state approximation when the free-stream Mach number is zero (see Balakrishnan 1999). In order to study the relative influence of the material derivatives on the stability, one of them was set equal to zero, while the Navier–Stokes approximation was used for the other. Neither of these approximations shown in columns 6 and 7 stabilized the Model 1 equations. With regard to the Woods equations, it must be noted that the absence of the material derivative $\mathscr{D}/\mathscr{D}t\,(\partial u_x/\partial x)$ in the Woods stress makes the approximations in columns 3 and 6 give the same linearized Woods equations when the free-stream Mach number is equal to zero. Also, the approximations in columns 5 and 7 make the resulting linearized Woods equations have the same structure.

4. Shock structure computations

The stable approximations to the material derivatives, as identified by the linearized stability analysis, do not guarantee that the complete set of nonlinear Model 1a and Model 1b equations will be entropy-consistent when applied to the shock structure problem. It would be difficult to establish such a causality, especially when two forms of the nonlinear Model 1 equations gave the same linearized Model 1 equations. The stable Euler and Navier–Stokes approximations to the material derivatives are used in the nonlinear Model 1a and Model 1b equations to solve the shock structure problem.

4.1. *Problem definition, numerical method and boundary conditions*

In the shock structure problem, the shock profiles are computed by specifying flow conditions at the upstream (inflow) and downstream (outflow) boundaries of a linear control volume that contains the normal shock. The length of the control volume was chosen to be an integral multiple of the upstream mean free path given by

$$\lambda_1 = \frac{16\mu_1}{5\rho_1\sqrt{2\pi RT_1}}, \tag{4.1}$$

where the subscripts 1 and 2 denote upstream and downstream conditions at $j = 1$ and $j = JMAX$, respectively. In these computations the grid points were not clustered

https://doi.org/10.1017/S0022112004007876 Published online by Cambridge University Press

in the vicinity of the shock. The hypersonic shock structure for argon was computed using the same flow conditions as Fiscko & Chapman (1988), that is:

$$\left.\begin{aligned} T_1 &= 300\,\mathrm{K}, \\ P_1 &= 1.01325 \times 10^5\,\mathrm{Nm}^{-2}, \\ \gamma &= 1.6666, \\ \mu_1 &= 22.7 \times 10^{-6}\,\mathrm{Nm}^{-2}. \end{aligned}\right\} \tag{4.2}$$

Along with these upstream flow conditions, the upstream Mach number is also specified and the downstream Mach number and other flow variables are obtained using the Rankine–Hugoniot conditions. In order to begin computations, the normal shock is located at the midpoint of the control volume by specifying upstream conditions for $j \leqslant JMID$ and downstream conditions for $j > JMID$. The BGK-Burnett equations were numerically integrated using an explicit hybrid scheme that employs a peculiar velocity upwinding kinetic scheme (see Rao & Deshpande 1995) for the Euler flux and central difference discretization for the Navier–Stokes and BGK-Burnett fluxes. Since the entropy consistency of the BGK-Burnett equations is in question, a first-order upwind scheme has been used to compute the shock structure. While it is well known that the first-order scheme is very dissipative, it does yield monotonic solutions that are wiggle free, thereby eliminating the possibility of entropy violations from the numerical scheme. Shock structure computations begin with the solution of the Navier–Stokes equations for $j \in (1, JMAX)$ in a control volume that is expected to contain the shock. The BGK-Burnett (and Burnett) equations were computed with an initial profile obtained from the converged Navier–Stokes solution. Since the inflow and outflow boundary conditions were specified, using the Rankine–Hugoniot conditions, there was no need to specify any other boundary condition, provided the control volume was large enough to contain the shock. In order to ascertain that there was no need for additional boundary conditions, the problem was solved by treating the outflow boundary as a subsonic boundary. This means that two of the characteristics are outgoing and one of them is incoming. The boundary conditions were applied by extrapolating the velocity and density from $j = JMAX - 1$ to $j = JMAX$ and specifying the downstream pressure at $j = JMAX$. These solutions were identical to the solutions obtained without explicitly specifying the outflow boundary conditions. In addition, the first-, second- and third-order derivatives were negligibly small at the boundaries of the control volume.

4.2. *BGK-Burnett Model 1a and Model 1b shock structure*

The shock structure was computed with the Burnett and Model 1a equations in a control volume of length $1000 \times \lambda_1$. In order to test for instabilities, the shock structure was computed by increasing the number of grid points until the equations became unsolvable. Increasing the number of grid points or decreasing the grid fineness ratio, defined as $\Delta x/\lambda_1$, increases the local Knudsen number. The material derivatives in the Model 1a equations were approximated by spatial derivatives from the Euler equations as these approximations stabilized the linearized Model 1 equations. In the Burnett equations, the $\partial^2\rho/\partial x^2$ term was dropped as suggested by Fiscko & Chapman (1988).

On very coarse grids, it was observed (as expected) that the solutions of the Navier–Stokes, Burnett and Model 1a equations were almost indistinguishable. However, as the grids were made finer, a negative entropy spike began to develop in the Burnett solutions just ahead of the shock. As shown in figures 5(*a*) and 5(*b*), the converged

https://doi.org/10.1017/S0022112004007876 Published online by Cambridge University Press

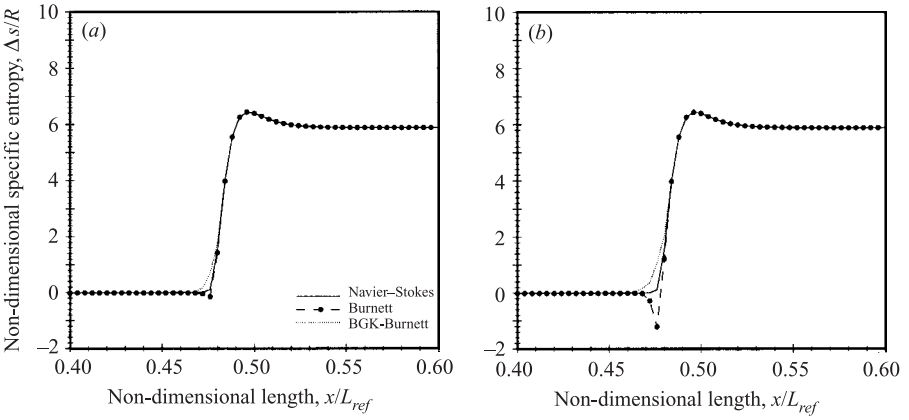


FIGURE 5. BGK-Burnett Model 1a and Burnett specific entropy variation across a Mach 20 normal shock in a monatomic hard sphere gas for (*a*) $\Delta x/\lambda_1 = 8.0$, (*b*) $\Delta x/\lambda_1 = 4.0$. The material derivatives $\mathscr{D}/\mathscr{D}t(\partial u_x/\partial x)$ and $\mathscr{D}/\mathscr{D}t\,(\partial T/\partial x)$ were approximated using the Euler equations. The Burnett equations failed at grid fineness ratios below the critical limit of $\Delta x/\lambda_1 = 4.0$. The critical grid fineness ratio of the Model 1a equations was lower than 4.0.

Burnett solutions for $M_1 = 20$ show a negative entropy spike just ahead of the shock. It must be noted, though, that the Burnett solutions did not break down at these grid fineness ratios. Increasing the number of grid points, increases the magnitude of the negative entropy spike until the temperature ahead of the shock becomes negative and the solution of the equations breaks down beyond this critical (limiting) grid fineness ratio. For the Burnett equations, the critical grid fineness ratio for $M_1 = 20$ is $\Delta x/\lambda_1 = 4.0$ and is lower for lower upstream Mach numbers. Although the Model 1a equations did not give rise to the negative entropy spike at these grid fineness ratios, it was observed that they too became unsolvable at grid fineness ratios that were slightly lower than the critical limit of $\Delta x/\lambda_1$ at which the Burnett equations became unsolvable. As a result, the performance of the Model 1a equations was only a marginal improvement on the Burnett equations. An increase in the number of grid points also necessitated lower CFL values until it became impossible to compute the Model 1a equations for grid fineness ratios less than unity. This instability was also observed when the upstream Mach number was reduced and the number of grid points was increased. In order to explain the instabilities experienced with increasing upstream Mach number and reducing grid fineness ratios, consider the definition of the cell Knudsen number

$$Kn_{\Delta x} = \frac{\lambda}{\Delta x} = 1.277M\frac{\sqrt{\gamma}}{Re_{\Delta x}}, \tag{4.3}$$

where $Re_{\Delta x}$ is the cell Reynolds number. The cell Knudsen number is also inversely proportional to the local fineness ratio $(\Delta x/\lambda)$, i.e. $Kn_{\Delta x} \propto \lambda/\Delta x$. An increase in the upstream Mach number and a corresponding lowering in the grid size causes an increase in the cell Knudsen number. Since the local Knudsen number, on fine grids, first, assumes values greater than unity on the upstream side of the shock, the Burnett and Model 1a equations fail in these regions.

With the inclusion of $\mathscr{D}v/\mathscr{D}t$ and $\partial v/\partial x$ in the stress and heat flux expressions of the Model 1b equations, computations were possible on grids that were finer than the grids used for Model 1a and Burnett equations. The material derivatives in the Model 1b equations were expressed using the Euler approximations and the Mach 5 normal

https://doi.org/10.1017/S0022112004007876 Published online by Cambridge University Press

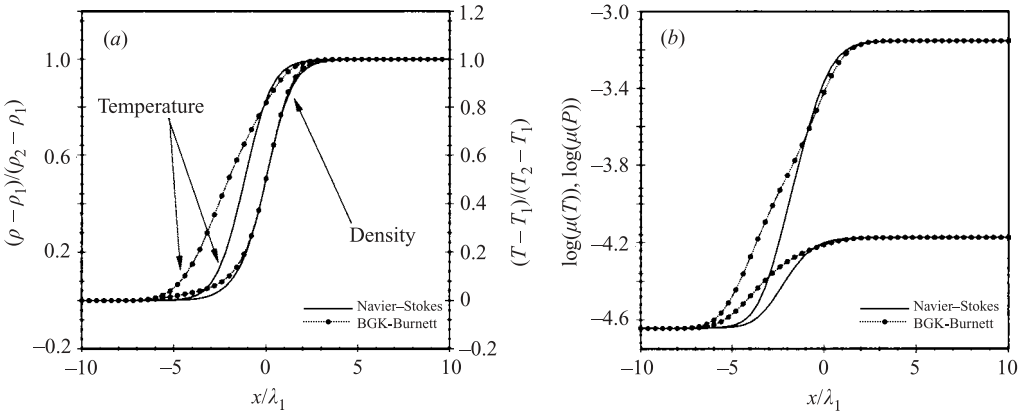


FIGURE 6. Comparison of the Model 1b and Navier–Stokes solutions for a Mach 5 normal shock in a monatomic hard sphere gas. These solutions were obtained on a mesh of critical fineness ratio $\Delta/\lambda = 0.4$ with Euler approximations to the material derivatives $\mathscr{D}/\mathscr{D}t(\partial u_x/\partial x)$ and $\mathscr{D}/\mathscr{D}t(\partial T/\partial x)$. (*a*) shows the variations of the normalized density and temperature and (*b*) shows the variations of $\breve{\mu}$ (denoted as $\mu(p)$) and $\mu(T)$ across the shock. Note the large variation in $\mu(p)$ as compared to the much smaller variation in $\mu(T)$ across the shock.

shock solutions, shown in figures 6(*a*) and 6(*b*), were obtained on a control volume that was $100\lambda_1$ wide with a grid fineness ratio $\Delta x/\lambda_1 = 0.4$. However, shock solutions were not obtainable on even finer grids, even with the Model 1b equations. It is shown in § 6 that despite Model 1b equations giving converged solutions that indicate a thicker shock than the Navier–Stokes solution, they are not entropy-consistent and consequently fail at grid fineness ratios lower than the critical ratio $\Delta x/\lambda_1 = 0.4$. For the Model 1a and Model 1b equations it was seen that using the Navier–Stokes approximations to the material derivatives did not improve the behaviour of the equations.

4.3. *The fictitious viscosity in the Model 1a equations*

A detailed examination of the Model 1a and Model 1b equations reveals that ignoring the contributions from $\mathscr{D}v/\mathscr{D}t$ and $\partial v/\partial x$ leads to differences in the viscosity in the first- and second-order fluxes in the Model 1a equations. In order to understand the cause of this difference, consider the Model 1a and Model 1b stress and heat flux given by equations (2.49), (2.50), (2.53) and (2.54). The inclusion of the $\mathscr{D}v/\mathscr{D}t$ and $\partial v/\partial x$ results in differences in the terms 1a, ..., 4a in equations (2.49) and (2.50) and the corresponding terms 1b, ..., 4b in equations (2.53) and (2.54). Rewriting the terms 1a, ..., 4a as

$$\frac{1}{\breve{\mu}}\frac{\mathscr{D}\breve{\mu}}{\mathscr{D}t} = \left(\frac{1}{\rho}\frac{\mathscr{D}\rho}{\mathscr{D}t} + \frac{1}{T}\frac{\mathscr{D}T}{\mathscr{D}t}\right), \quad \frac{1}{\breve{\mu}}\frac{\partial\breve{\mu}}{\partial x} = \left(\frac{1}{\rho}\frac{\partial\rho}{\partial x} + \frac{1}{T}\frac{\partial T}{\partial x}\right)$$

in equations (2.49) and (2.50), we define a fictitious viscosity

$$\breve{\mu} = \rho T, \tag{4.4}$$

which is proportional to the pressure. Using this definition, we rewrite the stress and

https://doi.org/10.1017/S0022112004007876 Published online by Cambridge University Press

heat flux terms in equations (2.49) and (2.50) as

$$\tau_{xx}^{B} = -\frac{\mu^2}{p}\left[2\Omega_1 \underbrace{\left(\frac{1}{\check{\mu}}\frac{\mathscr{D}\check{\mu}}{\mathscr{D}t}\right)}_{1a}\frac{\partial u_x}{\partial x} + 2\Omega_1\frac{\mathscr{D}}{\mathscr{D}t}\left(\frac{\partial u_x}{\partial x}\right) + 2\Omega_1\left(\frac{\partial u_x}{\partial x}\right)^2 - 4\Omega_2 R\frac{\partial^2 T}{\partial x^2} - 4\Omega_2 R\underbrace{\left(\frac{1}{\check{\mu}}\frac{\partial\check{\mu}}{\partial x}\right)}_{2a}\frac{\partial T}{\partial x}\right] \quad (4.5)$$

and

$$\dot{q}_x^{B} = \frac{\mu^2}{\rho}\left[\frac{4\Omega_3}{T}\underbrace{\left(\frac{1}{\check{\mu}}\frac{\mathscr{D}\check{\mu}}{\mathscr{D}t}\right)}_{3a}\frac{\partial T}{\partial x} + 4\Omega_4\underbrace{\left(\frac{1}{\check{\mu}}\frac{\partial\check{\mu}}{\partial x}\right)}_{4a}\frac{\partial u_x}{\partial x} + 4\Omega_4\frac{\partial^2 u_x}{\partial x^2} + \frac{4\Omega_3}{T}\frac{\mathscr{D}}{\mathscr{D}t}\left(\frac{\partial T}{\partial x}\right) + 4(\Omega_4 - \Omega_2 + \Omega_3)\frac{1}{T}\frac{\partial T}{\partial x}\frac{\partial u_x}{\partial x} + \frac{2\Omega_1}{RT}\frac{\mathscr{D}u_x}{\mathscr{D}t}\frac{\partial u_x}{\partial x}\right]. \quad (4.6)$$

Equations (2.53) and (2.54) may be obtained from the above equations by substituting μ in place of $\check{\mu}$. From equation (4.4), we notice that $\check{\mu}$ varies with pressure, while the constitutive relation for μ in the Navier–Stokes equations varies with temperature (see equation (2.55)). Figure 6(*b*) shows the large rise in $\check{\mu}$ (denoted by $\mu(p)$ in the figure) and the much smaller rise in $\mu(T)$ across the normal shock. This unphysical difference between $\check{\mu}(p)$, which is embedded in the Model 1a flux, and $\mu(T)$, the viscosity in the Navier–Stokes flux creates an abrupt jump in the viscosity between the first- and second-order fluxes that causes the BGK-Burnett Model 1a equations to become stiff as the grids are refined and the upstream Mach number is increased. It is because of this embedded fictitious viscosity that computations of the two-dimensional Model 1a equations for hypersonic flow about a blunt body (see Yun, Agarwal & Balakrishnan 1997) were not possible for free-stream Knudsen numbers greater than 0.01. However, in the BGK-Burnett Model 1b equations, the definition of viscosity is consistent throughout the first- and second-order fluxes and leads to an improved set of equations. To understand better the rationale for neglecting contributions from $\mathscr{D}v/\mathscr{D}t$ and $\partial v/\partial x$, consider figure 7. It is seen that for an $M_1 = 1.2$ normal shock, the increase in collision frequency across the shock is smaller than the corresponding rise across the $M_1 = 5$ shock. Also, the difference between $\check{\mu}(p)$ and $\mu(T)$ downstream of the shock increases with shock strength as shown by the viscosity variation across the $M_1 = 1.2$ and $M_1 = 5$ normal shocks in figure 7(*b*). It is conjectured that the problems associated with the Burnett equations are, in part, a result of this viscous imbalance. This can be seen from the fact that stress expressions in equations (2.51) and (2.58), and the heat flux expressions in equations (2.52) and (2.59) have identical derivatives. The inclusion of the material derivative of collision frequency in the formulation of the second-order flux, therefore, marks an important departure from all other formulations of second-order stress and heat flux approximations.

5. Boltzmann's H-theorem

The linearized stability analysis and shock structure computations identified stable approximations to the material derivatives and indicated the need for the $\mathscr{D}v/\mathscr{D}t$ and $\partial v/\partial x$ terms in the Model 1b stress and heat flux expressions. In order to assess

https://doi.org/10.1017/S0022112004007876 Published online by Cambridge University Press

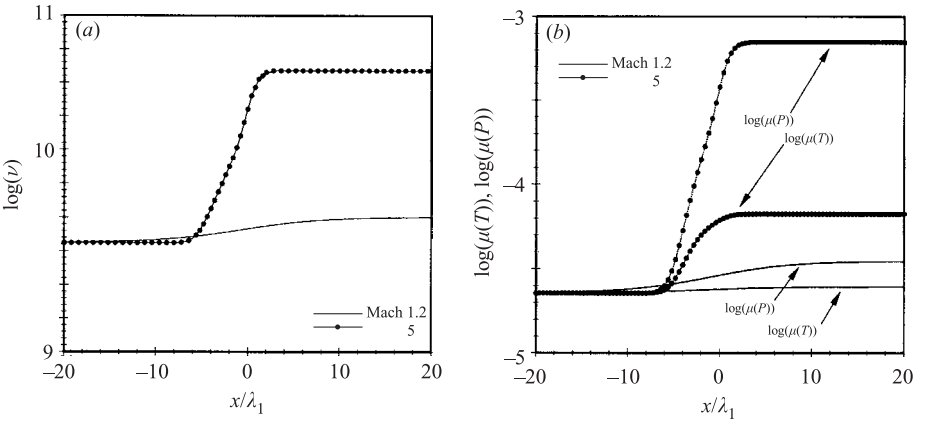


FIGURE 7. Collision frequency ν and molecular viscosity $\mu(p)$ and $\mu(T)$ variations across a Mach 1.2 and Mach 5 normal shock. (*a*) ν variation, (*b*) $\mu(p)$ and $\mu(T)$ variations. An increase in the upstream Mach number makes the difference between $\breve{\mu}$ and μ large.

the entropy consistency of second-order hydrodynamic equations it is required to calculate the irreversible entropy produced by the equations. The classical equation for the change in entropy, i.e. $\Delta s = c_v \log(T_2/T_1) - R\log(\rho_2/\rho_1)$, used in § 4 to correlate the formation of the negative entropy spike with the resulting instability (see figure 5), follows from the Gibbs equation (5.6) that is applicable only to systems in thermodynamic equilibrium. Since the BGK-Burnett equations model a gas in a state of collisional and translational non-equilibrium, it is required that the expression for the entropy includes second-order departures from equilibrium. Boltzmann's H-theorem generalizes the concept of entropy by making explicit the manner in which a system evolves from an arbitrary initial state. In its original unrestricted form (see ter Haar 1956), the H-theorem states that any system will tend towards equilibrium if equilibrium conditions did not exist to begin with. For a spatially inhomogeneous gas, Grad (see Haviland 1962) has shown that the inequality

$$\frac{\partial H}{\partial t} + \frac{\partial H_v}{\partial x} \leqslant 0 \tag{5.1}$$

must be satisfied when the gas approaches equilibrium. The definition of the H function and H_v in (5.1) is modified to include contributions from the non-translational modes of energy (see Deshpande 1986) and is given by

$$H = \int_{\mathbb{R}^+}\int_{\mathbb{R}} \left(f \log_e f + \frac{5-3\gamma}{2(\gamma-1)} f \log_e \beta \right) \mathrm{d}v_x \, \mathrm{d}I, \tag{5.2}$$

$$H_v = \int_{\mathbb{R}^+}\int_{\mathbb{R}} v_x \left(f \log_e f + \frac{5-3\gamma}{2(\gamma-1)} f \log_e \beta \right) \mathrm{d}v_x \, \mathrm{d}I. \tag{5.3}$$

For monatomic gases, $\gamma = 5/3$, the integrand in the expressions for H and H_v reduce to the standard expression $f \log_e f$. By taking moments of the Boltzmann equation with the linear combination of collision invariants

$$\left\langle -R\left(1 + \log_e f - 2\frac{(5-3\gamma)}{(3-\gamma)}\beta I\right), \frac{\partial f}{\partial t} + v_x \frac{\partial f}{\partial x} \right\rangle = \left\langle -R\left(1 + \log_e f - 2\frac{(5-3\gamma)}{(3-\gamma)}\beta I\right), \nu\left(f^{(0)} - f\right) \right\rangle, \tag{5.4}$$

https://doi.org/10.1017/S0022112004007876 Published online by Cambridge University Press

equation (5.1) can, after simplification, be recast as an entropy balance equation

$$\rho \frac{\mathscr{D}s}{\mathscr{D}t} + \nabla \cdot \boldsymbol{J} = \dot{\sigma}, \tag{5.5}$$

where $s = -RH$ is the specific entropy, $\boldsymbol{J}$ is the entropy flux and $\dot{\sigma}$ denotes the rate of production of irreversible entropy. Equation (5.5) is similar to the Gibbs entropy balance equation from equilibrium thermodynamics

$$\rho \frac{\mathscr{D}s_{eq}}{\mathscr{D}t} + \frac{\partial}{\partial x}\left(\frac{\dot{q}_x}{T}\right) = \frac{1}{T}\tau_{xx}\left(\frac{\partial u_x}{\partial x}\right) - \frac{\dot{q}_x}{T^2}\left(\frac{\partial T}{\partial x}\right) \geqslant 0 \tag{5.6}$$

$$\rho \frac{\mathscr{D}s_{eq}}{\mathscr{D}t} + \nabla \cdot \boldsymbol{J}_{eq} = \dot{\sigma}_{eq} \tag{5.7}$$

where $\boldsymbol{J}_{eq} = \dot{\boldsymbol{q}}/T$ denotes the entropy flux and the source term

$$\dot{\sigma}_{eq} = \frac{1}{T}\tau_{xx}\left(\frac{\partial u_x}{\partial x}\right) - \frac{\dot{q}_x}{T^2}\left(\frac{\partial T}{\partial x}\right) \tag{5.8}$$

denotes the rate of production of irreversible entropy, which must be either positive or zero in accordance with the second-law of thermodynamics. For a Maxwellian distribution function it can shown that $\Delta s^{(0)} = \Delta s_{eq} = c_v \log(T_2/T_1) - R\log(\rho_2/\rho_1)$ and the irreversible entropy produced equals zero ($\dot{\sigma}^{(0)} = 0$). It can be shown (see Comeaux 1995; Balakrishnan 1999) that for monatomic hard sphere gases, the expressions for $\dot{\sigma}$ and $\dot{\sigma}_{eq}$ are identical only up to first-order departures from equilibrium. Therefore, the entropy consistency of second-order distribution functions is verified by evaluating

$$\frac{\mathscr{D}s}{\mathscr{D}t} + \nabla \cdot \boldsymbol{J} = \left\langle -R\nu\left(f^{(0)} - f\right)\left[1 + \log_e f - \frac{2(5-3\gamma)}{(3-\gamma)}\beta I\right]\right\rangle \tag{5.9}$$

and checking if the source term on the right-hand side is greater than zero. From equation (5.9), the production of irreversible entropy for second-order departures from equilibrium is given by (see Balakrishnan (1999) for details regarding this derivation)

$$\begin{aligned}
\dot{\sigma} &= \dot{\sigma}^{(1)} + \dot{\sigma}^{(2)} \\
&= \mu R\left[E_1^{(1)}\frac{1}{T^2}\left(\frac{\partial T}{\partial x}\right)^2 + E_2^{(1)}\frac{1}{RT}\left(\frac{\partial u_x}{\partial x}\right)^2\right] + \frac{\mu^2 R}{p^2}\left[E_1^{(2)}R\frac{\rho}{T}\frac{\partial T}{\partial x}\frac{\mathscr{D}}{\mathscr{D}t}\left(\frac{\partial T}{\partial x}\right)\right. \\
&\quad + E_2^{(2)}R\frac{\rho}{T}\frac{\partial u_x}{\partial x}\left(\frac{\partial T}{\partial x}\right)^2 + E_3^{(2)}\rho\left(\frac{\partial u_x}{\partial x}\right)^3 + E_4^{(2)}\rho\left(\frac{\partial u_x}{\partial x}\right)\frac{\mathscr{D}}{\mathscr{D}t}\left(\frac{\partial u_x}{\partial x}\right) \\
&\quad \left. + E_5^{(2)}R\rho\frac{\partial T}{\partial x}\frac{\partial^2 u_x}{\partial x^2} + E_6^{(2)}R\rho\frac{\partial u_x}{\partial x}\frac{\partial^2 T}{\partial x^2} + E_7^{(2)}R\frac{\partial \rho}{\partial x}\frac{\partial u_x}{\partial x}\frac{\partial T}{\partial x}\right],
\end{aligned} \tag{5.10}$$

where the coefficients $E_j^{(i)}$ are given in tables 7 and 8. In equation (5.10), the irreversible entropy generated by the first-order terms in the distribution function is given by the terms of order $O(\mu)$ that are denoted by $\dot{\sigma}^{(1)}$. The irreversible entropy generated by the second-order terms in the distribution function is given by the $O(\mu^2)$ terms denoted by $\dot{\sigma}^{(2)}$. The material derivatives present in $\dot{\sigma}^{(2)}$ and the material derivatives in the Model 1 stress and heat flux are the same. When the Euler equations are used to approximate the material derivatives, terms up to $O(\mu^2)$ are present in the expression for $\dot{\sigma}$. When the same material derivatives are approximated using the Navier–Stokes equations there are additional terms that are of $O(\mu^3)$.

https://doi.org/10.1017/S0022112004007876 Published online by Cambridge University Press

$$E_1^{(1)} = \varphi_1, \qquad E_2^{(1)} = \varphi_2, \qquad \boldsymbol{E_1^{(2)} = -2\varphi_1},$$
$$\boldsymbol{E_2^{(2)} = 2(\omega(\gamma-1)-1)\varphi_1 - 2(1+\omega)\varphi_3 + 2(\omega-1)\varphi_4 + 2\varphi_5 + 2\varphi_6 + \varphi_7},$$
$$\boldsymbol{E_3^{(2)} = 2(\omega(\gamma-1)-1)\varphi_2 + \varphi_8}, \quad \boldsymbol{E_4^{(2)} = -2\varphi_2},$$
$$\boldsymbol{E_5^{(2)} = -2\varphi_3}, \quad \boldsymbol{E_6^{(2)} = 2\varphi_4}, \qquad \boldsymbol{E_7^{(2)} = 2\varphi_5}$$

TABLE 7. The $E_j^{(i)}$ coefficients in the non-equilibrium formulation of the first- and second-order irreversible entropy production terms in the BGK-Burnett equations. In order to distinguish the second-order entropy coefficients from the first-order coefficients, the former is shown using boldface characters.

$$\varphi_1 = \tfrac{5}{2} \qquad \varphi_2 = \tfrac{1}{2}(3\gamma^2 - 10\gamma + 11)$$
$$\varphi_3 = 6\left(\tfrac{1}{4}\theta_4 + \theta_5\right) \qquad l_1 = \tfrac{1}{4}(3\gamma - 5)(2\theta_1 + 2\theta_2 + 3\theta_3)$$
$$l_2 = \tfrac{1}{4}(3-\gamma)(6\theta_1 + 6\theta_2 + 15\theta_3) \qquad l_3 = \tfrac{1}{2}(\gamma - 1)(2\theta_1 + 4\theta_2 + 3\theta_3)$$
$$\varphi_4 = l_1 + l_2 - l_3 \qquad \varphi_5 = \tfrac{1}{2}(11 - 5\gamma)$$
$$l_4 = \tfrac{3}{2}\theta_1 + 2\theta_2 + \tfrac{9}{2}\theta_3 \qquad l_5 = \tfrac{15}{8}\theta_4 + \tfrac{5}{4}\theta_5 + \tfrac{5}{4}\theta_6$$
$$l_6 = \tfrac{3}{8}(3-\gamma)(2\theta_1 + 2\theta_2 + 5\theta_3) \qquad l_7 = \tfrac{1}{4}(\gamma - 1)(2\theta_1 + 4\theta_2 + 3\theta_3)$$
$$\varphi_6 = l_4 - l_5 + l_6 - l_7 \qquad \varphi_7 = \tfrac{3}{2}(37 - 15\gamma)$$
$$\varphi_8 = -(3\gamma^3 - 15\gamma^2 + 33\gamma - 29)$$

TABLE 8. Coefficients in the first- and second-order non-equilibrium irreversible entropy production terms in the BGK-Burnett equations.

5.1. *Assessing the entropy consistency of the Model 1b equations*

It can be seen that $\dot{\sigma}^{(1)}$ is always positive and this leads to the assertion that the Navier–Stokes equations are entropy-consistent. However, the large number of derivatives that are present in $\dot{\sigma}^{(2)}$ necessitates a computational evaluation of $\dot{\sigma}$ to determine if the BGK-Burnett equations satisfy the second-law of thermodynamics.

5.1.1. $M_1 = 1.2$ *normal shock*

To demonstrate the calculation of $\dot{\sigma}$, the Model 1b equations were solved for a weak normal shock with upstream Mach number $M_1 = 1.2$. This computation was based on the flow conditions given in (4.2). The computations were carried out on a control volume of length $100\lambda_1$. The material derivatives in the Model 1b stress and heat flux were represented by the two sets of approximations. In the first set, the material derivatives $\mathscr{D}/\mathscr{D}t\,(\partial u_x/\partial x)$ and $\mathscr{D}/\mathscr{D}t\,(\partial T/\partial x)$ were expressed using the stable Euler approximations. The converged Model 1b and Navier–Stokes solutions on a grid of fineness ratio $\Delta x/\lambda_1 = 0.2$ are shown in figure 8(*a*). The converged Model 1b solution was used to compute the derivatives in entropy production term in equation (5.10). Since the Euler approximations were used to express the material derivatives, the same approximations were used to compute the derivatives in equation (5.10). The entropy production in the control volume is shown in figures 8(*a*). Even at this low upstream Mach number, it is seen that $\dot{\sigma}^{(2)}$ is negative near the upstream region of the shock. However, the large positive value of $\dot{\sigma}^{(1)}$ makes the total value

https://doi.org/10.1017/S0022112004007876 Published online by Cambridge University Press

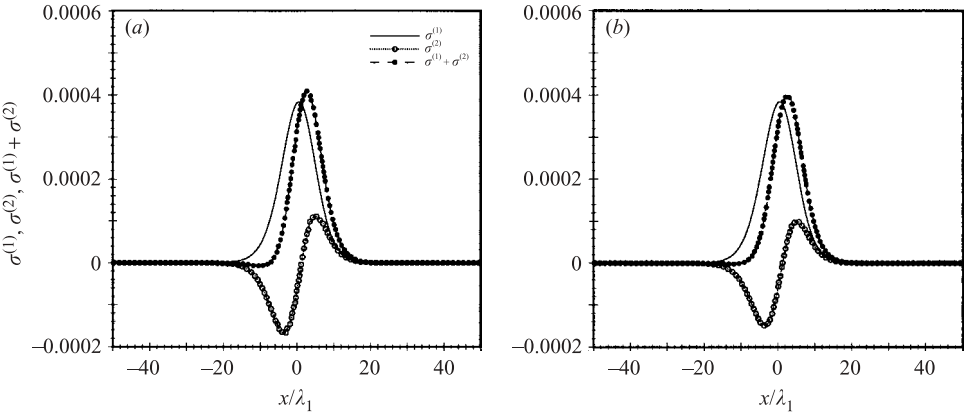


FIGURE 8. Entropy production by the BGK-Burnett Model 1b equations for a $M_1 = 1.2$ normal shock in a monatomic hard sphere gas. The grid fineness ratio used in this computation was $\Delta x/\lambda_1 = 0.2$. In (*a*) the stable Euler approximations were used for the material derivatives $\mathscr{D}/\mathscr{D}t\,(\partial u_x/\partial x)$ and $\mathscr{D}/\mathscr{D}t\,(\partial T/\partial x)$. In (*b*) the unstable Navier–Stokes approximation was used for the material derivative $\mathscr{D}/\mathscr{D}t\,(\partial u_x/\partial x)$ and $\mathscr{D}/\mathscr{D}t\,(\partial T/\partial x) = 0$. Both sets of approximations gave converged solutions that are also entropy consistent.

of $\dot{\sigma}$ positive throughout the computational domain and the solution is, therefore, entropy-consistent.

In the second set, the material derivative $\mathscr{D}/\mathscr{D}t\,(\partial u_x/\partial x)$ was expressed using the Navier–Stokes approximation and the material derivative $\mathscr{D}/\mathscr{D}t\,(\partial T/\partial x) = 0$. From table 6, we see that this choice of approximating the material derivatives is unstable. However, in this case too, the Model 1b equations gave a converged solution on a grid of fineness ratio $\Delta x/\lambda_1 = 0.2$ shown in figure 8(*b*). Once again, with the same material derivative approximations used to evolve the equations, the converged Model 1b solution was used to compute the derivatives in entropy production term in equation (5.10). It is seen that this solution also generates a positive entropy throughout the control volume. For these computations an initial profile specified using the Rankine–Hugoniot relations and converged Navier–Stokes solution gave identical results.

5.1.2. $M_1 = 5$ *normal shock*

In § 4, it was mentioned that the solution of the Model 1b equations with the Euler approximations failed to converge for grid fineness ratios below the critical value of $\Delta x/\lambda_1 = 0.4$ (see figure 6*a*). In order to test the entropy consistency of the equations for an $M_1 = 5$ shock, the converged solution at $\Delta x/\lambda_1 = 0.4$ was used to compute the irreversible entropy produced by the equations. The plot of the irreversible entropy in figure 9(*a*) shows that the $\dot{\sigma}^{(1)}$ terms in equation (5.10) are positive throughout the domain. However, the $\dot{\sigma}^{(2)}$ terms are negative in much of the shock and further, the combined entropy $\dot{\sigma}^{(1)} + \dot{\sigma}^{(1)}$ is negative. An important point that should be emphasized is that despite the fact that the Model 1b equations generated negative irreversible entropy at this grid fineness ratio, the temperature of the gas did not become negative yet for the numerical solution to fail. Hence, it was possible to obtain converged solutions at $\Delta x/\lambda_1 = 0.4$. However, lowering the grid fineness ratio below the critical value causes the temperature to become negative and the equations fail.

https://doi.org/10.1017/S0022112004007876 Published online by Cambridge University Press

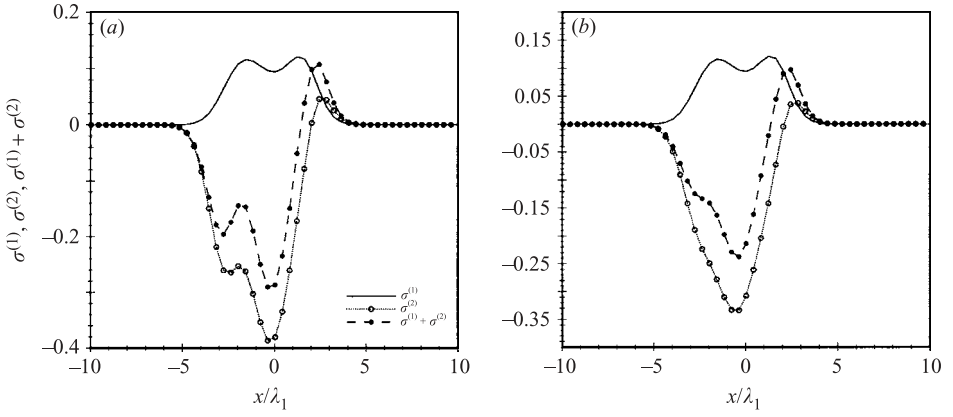


FIGURE 9. Variation of $\dot{\sigma}^{(1)}$, $\dot{\sigma}^{(2)}$ and $\dot{\sigma}^{(1)} + \dot{\sigma}^{(2)}$ for the Model 1b equations. The flow conditions are $M_1 = 5$ and $\Delta x/\lambda_1 = 0.4$. In (*a*) the Navier–Stokes approximations were used for $\mathscr{D}/\mathscr{D}t\,(\partial u_x/\partial x)$ and $\mathscr{D}/\mathscr{D}t\,(\partial T/\partial x)$. The variations, based on a converged solution, show that the equations are entropy inconsistent at this critical grid fineness ratio. In (*b*) the Navier–Stokes approximation was used for $\mathscr{D}/\mathscr{D}t\,(\partial u_x/\partial x)$ and $\mathscr{D}/\mathscr{D}t\,(\partial T/\partial x) = 0$. The Model 1b equations did not yield a converged solution even on coarse grids. The variations in this case were based on an intermediate profile just before the equations failed on a $\Delta x/\lambda_1 = 0.4$ grid.

In figure 9(*b*), the Navier–Stokes approximation was used for $\mathscr{D}/\mathscr{D}t\,(\partial u_x/\partial x)$ and $\mathscr{D}/\mathscr{D}t\,(\partial T/\partial x) = 0$. This approximation was shown to be unstable (see table 6) and failed to produce a converged solution for the $M_1 = 5$ normal shock, even on coarse grids. An examination of the intermediate shock profile, obtained just before the equations broke down, reveals that the irreversible entropy produced is negative for much of the region of the shock. For these approximations, the temperature of the gas becomes negative as the solution evolves on even coarse grids. Hence, it was not possible to obtain converged solutions on any grid.

6. Entropy-consistent approximations to the material derivatives

The formulation of entropy-consistent BGK-Burnett equations requires that the converged BGK-Burnett solutions generate a positive $\dot{\sigma}$. However, the BGK-Burnett equations must be entropy-consistent to yield a converged solution. These contradictory requirements present a paradox. Further, the analysis of the Model 1b equations has been based on the identification of stable approximations to the material derivatives followed by computation of the shock structure with the Model 1b equations in which the material derivatives were represented by the stable approximations. Since the closure coefficients are non-unique, the application of the two steps in the identification methodology (see figure 2) to each set of closure coefficients is a very time-consuming way of identifying BGK-Burnett equations that are entropy-consistent. From the entropy analysis of the $M_1 = 1.2$ and $M_1 = 5$ normal shock computations, we make the following observations:

(i) For weak shocks, the stable as well as unstable approximations to the material derivative yields entropy-consistent solutions on very fine grids.

(ii) For medium to high upstream Mach numbers, the stable approximations to the material derivatives made the Model 1b equations entropy inconsistent below a critical grid fineness ratio.

https://doi.org/10.1017/S0022112004007876 Published online by Cambridge University Press

(iii) For strong shocks, the Model 1b equations with unstable approximations to the material derivatives broke down on even relatively coarse grids. Further, an analysis of the intermediate shock profile before the equations broke down revealed that the profile was entropy inconsistent.

(iv) While the $M_1 = 1.2$ Model 1b solutions could be obtained using the Rankine–Hugoniot relations to specify the initial conditions, the solution of the $M_1 = 5$ shock required a converged Navier–Stokes solution as the initial profile.

Since the BGK-Burnett solution may be viewed as a second-order relaxation of the Navier–Stokes solution, it is conjectured that the Navier–Stokes solution would have developed as an intermediate profile of the BGK-Burnett equations had the latter been started on an initial profile specified by the Rankine–Hugoniot relations. Based on these observations we propose the entropy-consistent relaxation technique to identify entropy-consistent approximations to the material derivatives.

Entropy-Consistent Relaxation Technique (ECRT). The central idea behind this technique is that by considering the Navier–Stokes solution to be an entropy-consistent intermediate profile of the BGK-Burnett solution, it is possible to identify approximations to the material derivatives in τ_{xx}^B and $\dot{q}_x^B$ which will preserve the positivity of the irreversible entropy as the BGK-Burnett solution evolves.

The ECRT requires that the BGK-Burnett solutions do not violate the second-law of thermodynamics at any stage during the evolution process.

6.1. *Applying the entropy-consistent relaxation technique to the Model 1b equations*

The entropy-consistent relaxation technique is applied by computing $\dot{\sigma}$ from a converged Navier–Stokes solution. The material derivatives in equation (5.10) are expressed by using the stable approximations that were identified by the linearized stability analysis. The approximations to the material derivatives that generate positive $\dot{\sigma}$ are considered to be candidate entropy-consistent approximations to the material derivatives in the second-order stress and heat flux expressions. The BGK-Burnett Model 1b equations with these candidate approximations are computed from the initial profile obtained from the converged Navier–Stokes solution. If the converged Model 1b solution is entropy-consistent (positive $\dot{\sigma}$) then these approximations are used to define the constitutive relations for the second-order fluxes in the entropy-consistent BGK-Burnett equations.

6.1.1. $M_1 = 1.2$ *normal shock*

The ECRT, described above, was applied to the solution of the $M_1 = 1.2$ shock structure with the Model 1b equations. The approximations to the material derivatives that were stable to small wavelength perturbations were used to compute $\dot{\sigma}$ from a converged Navier–Stokes solution of the $M_1 = 1.2$ shock structure. To illustrate this, we consider the stable Navier–Stokes approximations to the material derivatives. From figure 10, we see that the irreversible entropy generated from the converged Navier–Stokes solution is positive throughout the computational domain. Hence, the stable Navier–Stokes approximation to the material derivatives in the Model 1b equations is used to evolve the shock structure. The converged Model 1b solution is used to compute $\dot{\sigma}$ which is seen in figure 10(b) to be positive throughout the region of the shock. Similar results were obtained when the ECRT was applied to the stable Euler approximations to the material derivatives. Since the Navier–Stokes approximation adds a third-order term to the expression for $\dot{\sigma}$ and the Model 1b fluxes, the solutions of the Model 1b equations with the Euler approximations in figure 8(a) and the Navier–Stokes approximations in figure 10(b) are almost identical.

https://doi.org/10.1017/S0022112004007876 Published online by Cambridge University Press

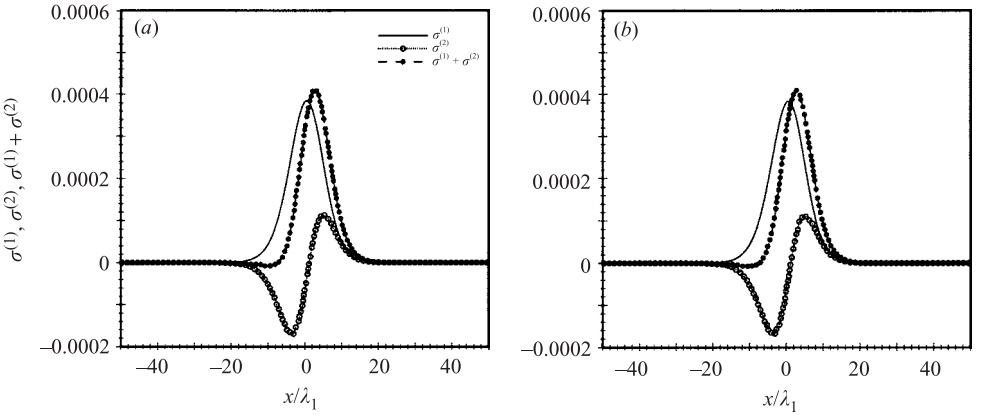


FIGURE 10. Variation of $\dot{\sigma}^{(1)}$, $\dot{\sigma}^{(2)}$ and $\dot{\sigma}^{(1)}+\dot{\sigma}^{(2)}$ for the Navier–Stokes and Model 1b equations across a Mach 1.2 normal shock in a monatomic hard sphere on a grid of $\Delta x/\lambda_1 = 0.2$. The stable Navier–Stokes approximations were used to express the material derivatives $\mathscr{D}/\mathscr{D}t$ $(\partial u_x/\partial x)$ and $\mathscr{D}/\mathscr{D}t\,(\partial T/\partial x)$. (*a*) $\dot{\sigma}$ variation based on the converged Navier–Stokes solution that was the initial solution for the Model 1b computations, (*b*) $\dot{\sigma}$ variation based on the converged Model 1b computations. For this Mach number and grid fineness ratio the Model 1b equations are entropy-consistent.

Also, from figure 10, we note that for this weak shock, the converged Navier–Stokes and Model 1b solutions are almost identical.

6.1.2. $M_1 = 5$ *normal shock*

The ECRT was applied to the solution of the Mach 5 shock structure with the Model 1b equations. The approximations to the material derivatives that were stable to small wavelength perturbations were used to compute $\dot{\sigma}$ from a converged Navier–Stokes solution of the $M_1 = 5$ shock structure. It was noticed that the stable Navier–Stokes approximations to the material derivatives generated negative $\dot{\sigma}$ in the region of the shock when $\dot{\sigma}$ was computed based on converged Navier–Stokes and Model 1b solutions for the critical grid fineness ratio $\Delta x/\lambda_1 = 0.4$. Similar results were obtained using the Euler approximations to the material derivatives as in figure 9(*a*). Also, by using the unstable Navier–Stokes approximation for $\mathscr{D}/\mathscr{D}t(\partial u_x/\partial x)$ and setting $\mathscr{D}/\mathscr{D}t(\partial T/\partial x) = 0$ in equation (5.10), we see, from figure 12(*b*), that $\dot{\sigma}$ generated by the converged Navier–Stokes solution is negative. The evolution of the Model 1b equations with this unstable and entropy inconsistent approximations breaks down on even coarse grids. The variations in figures 10 and 11 highlight an important point, namely that, material derivative approximations that generate negative irreversible entropy based on the converged Navier–Stokes solution do not produce entropy-consistent BGK-Burnett solutions.

Based on this observation, we narrow our search for entropy-consistent approximations to the material derivatives by considering only stable approximations that generate positive $\dot{\sigma}$ from an initial profile based on the converged Navier–Stokes solution. Since the Model 1b equations are found to violate the second-law of thermodynamics, we apply the ECRT to the Model 2 equations that are derived from another set of closure coefficients.

https://doi.org/10.1017/S0022112004007876 Published online by Cambridge University Press

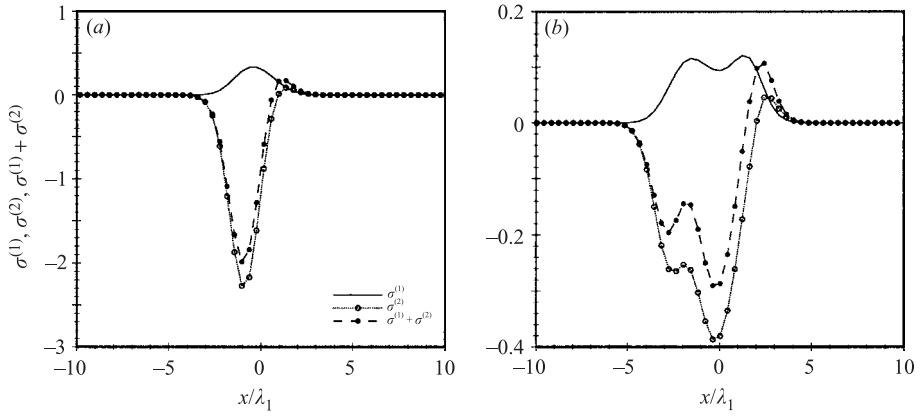


FIGURE 11. Variation of $\dot{\sigma}^{(1)}$, $\dot{\sigma}^{(2)}$ and $\dot{\sigma}^{(1)}+\dot{\sigma}^{(2)}$ for the Model 1b equations. The flow conditions are $M_1=5$ and $\Delta x/\lambda_1=0.4$. The Navier–Stokes approximations were used for $\mathscr{D}/\mathscr{D}t$ $(\partial u_x/\partial x)$ and $\mathscr{D}/\mathscr{D}t\,(\partial T/\partial x)$. (*a*) The variations based on the converged Navier–Stokes solution. (*b*) The variations based on the converged Model 1b solution. For this Mach number and grid fineness ratio the Navier–Stokes approximations are entropy inconsistent. For grid fineness ratios smaller than 0.4, the Model 1b equations failed to give a converged solution.

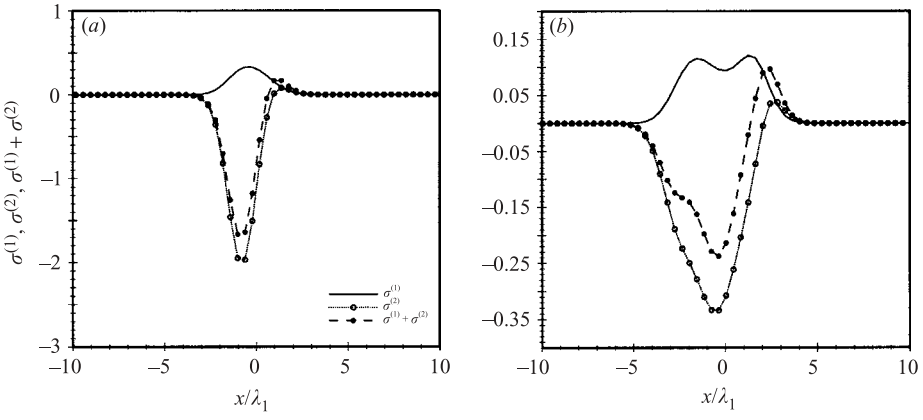


FIGURE 12. Variation of $\dot{\sigma}^{(1)}$, $\dot{\sigma}^{(2)}$ and $\dot{\sigma}^{(1)}+\dot{\sigma}^{(2)}$ for the Model 1b equations. The flow conditions are $M_1=5$ and $\Delta x/\lambda_1=0.4$. The Navier–Stokes approximation was used for $\mathscr{D}/\mathscr{D}t$ $(\partial u_x/\partial x)$ and $\mathscr{D}/\mathscr{D}t\,(\partial T/\partial x)=0$. (*a*) The variations based on the converged Navier–Stokes solution. (*b*) The variations based on a solution of the Model 1b equations just before the equations broke down.

7. Model 2: an improved set of BGK-Burnett equations

7.1. *Formulation of the Model 2 equations*

The derivation of the BGK-Burnett equation makes it clear that the entropy consistency of the equations depends on the closure coefficients and the approximations to the material derivatives. The previous sections identified the fictitious viscosity that is created when $\mathscr{D}v/\mathscr{D}t$ and $\partial v/\partial x$ are neglected and explored the entropy consistency of the Model 1b equations by computing $\dot{\sigma}$ for various approximations to the material derivatives. The use of the ECRT to identify stable approximations that were also entropy-consistent did not yield an entropy-consistent set of Model 1b equations for shock structure computations for upstream Mach numbers $M_1=5$ and higher.

https://doi.org/10.1017/S0022112004007876 Published online by Cambridge University Press

$$\omega_1 = \frac{97\gamma - 135}{4(9 - 7\gamma)} \qquad \omega_2 = -\frac{23\gamma - 27}{2(9 - 7\gamma)} \qquad \breve{\omega}_1 = \frac{17\gamma - 27}{2(9 - 7\gamma)}$$
$$\theta_1 = \tfrac{5}{2} + \omega_1 \qquad \theta_2 = \omega_2 - 1 \qquad \theta_3 = -(1 + \breve{\omega}_1)$$
$$\theta_4 = (3 - \gamma) + \omega_3 \qquad \theta_5 = -(\gamma - 1) - \omega_3 \qquad \theta_6 = \frac{(3\gamma - 5)}{2} + \omega_3$$

TABLE 9. Closure coefficients of the Model 2 second-order distribution function (7.1). These closure coefficients are functions of the specific heat ratio γ of the gas. Since the closure function $\widetilde{\mathscr{B}}^{(2)}(I, C_x)$ of the Model 2 equations is the same as that of the Model 1 equations, the functional form of the closure coefficient ω_3 is the same as that given in table 1.

Therefore, it was conjectured that the requirement of moment closure alone may not give rise to an entropy-consistent set of equations and that additional constraints may be required to evaluate the closure coefficients. In the formulation of the Model 2 equations, an additional constraint was imposed by requiring that the stability trajectories of the linearized BGK-Burnett and Navier–Stokes equations look similar. On comparing the characteristic polynomials of the linearized BGK-Burnett and Navier–Stokes equations and exploring the relative influence of the various coefficients on the stability, it was noticed that the closure function $\widetilde{\mathscr{B}}^{(2)}(I, C_x)$ has a less pronounced effect on the stability of the linearized equations than the closure function $\widetilde{\mathscr{B}}^{(1)}(I, C_x)$. The modified closure function $\widetilde{\mathscr{B}}^{(1)}(I, C_x)$ takes the form

$$\widetilde{\mathscr{B}}^{(1)}(I, C_x) = \frac{1}{\beta}\left(\tfrac{5}{2} + \omega_1\right) C_x^2 + \frac{1}{\beta}\frac{I}{I_0}(\omega_2 - 1) C_x^2 - (1 + \breve{\omega}_1) C_x^4, \tag{7.1}$$

where closure coefficients that satisfy the moment closure relation (2.22) are given in table 9. The second-order distribution function is given by

$$f = f^{(0)} + \xi f^{(1)} - \frac{\xi}{\nu}\left[\frac{\partial}{\partial t}\left(f^{(1)}\right) + \frac{\partial}{\partial x}\left(u_x f^{(1)}\right) + \frac{\partial}{\partial x}\left(f^{(0)}\widetilde{\phi}^{(1)}\right)\right], \tag{7.2}$$

where

$$\left.\begin{aligned} \widetilde{\phi}^{(1)} &= -\frac{1}{\xi\nu}\left[\widetilde{\mathscr{B}}^{(1)}(I, C_x)\frac{\partial\beta}{\partial x} + \widetilde{\mathscr{B}}^{(2)}(I, C_x)\frac{\partial u_x}{\partial x}\right], \\ \widetilde{\mathscr{B}}^{(1)}(I, C_x) &= \frac{\theta_1}{\beta}C_x^2 + \theta_2\frac{I}{\beta I_0}C_x^2 + \theta_3 C_x^4, \\ \widetilde{\mathscr{B}}^{(2)}(I, C_x) &= \theta_4\beta C_x^3 + \theta_5\frac{I}{I_0}C_x + \theta_6 C_x, \end{aligned}\right\} \tag{7.3}$$

Since equation (7.3) is identical to equation (2.43), the second-order flux in Model 2 is given by the generic expressions (2.47) and (2.48). In the formulation of Model 2b flux, the material and spatial derivatives of the collision frequency were retained. Hence, the derivatives in the stress and heat flux terms of the Model 2b equations are identical to the derivatives in the Model 1b flux. Also, the functional form of the expressions for the stress and heat flux coefficients are identical to that of the Model 1 equations given in table 2. The numerical values are quite different, though, as the closure coefficients for the Model 2 equations are quite different. A comparison of the Model 2 stress and heat flux coefficients with the corresponding coefficients in the Model 1b, Burnett and Woods equations is shown in table 10. Unlike

https://doi.org/10.1017/S0022112004007876 Published online by Cambridge University Press

$\tau_{xx}^{(II)}$ and $\dot{q}_x^{(II)}$	BGK-Burnett Model 1b	BGK-Burnett Model 2b	Burnett	Woods
A_1	0.889	0.889	2.6667	4.444
A_2	1.333	1.333	1.3333	0
A_3	0	0	0.0	0
A_4	**−4.5**	**2.25**	**2.0**	**2.0**
A_5	**−2.25**	**1.125**	**1.0**	**1.0**
B_1	**−2.833**	**3.9167**	**22.125**	**33.5**
B_2	2.5	2.5	5.625	11.25
B_3	0.889	0.889	2.0	0
B_4	−1.333	−1.333	−2.0	0

TABLE 10. A comparison of the Model 1b, Model 2b, Burnett and Woods stress and heat flux coefficients for a monatomic hard sphere gas, i.e. $\gamma = 1.6666$ and $\omega = 0.5$. Boldface characters highlight the change in the sign of the A_4, A_5 and B_1 coefficients in the Model 1b and Model 2b equations. Also, the non-zero Model 2b, Burnett and Woods stress and heat flux coefficients have the same sign.

	Exact (no approx.) for $\mathscr{D}/\mathscr{D}t(\mathscr{A})$ $\mathscr{D}/\mathscr{D}t(\mathscr{B})$	Steady state for $\mathscr{D}/\mathscr{D}t(\mathscr{A})$ $\mathscr{D}/\mathscr{D}t(\mathscr{B})$	Euler based approx. for $\mathscr{D}/\mathscr{D}t(\mathscr{A})$ $\mathscr{D}/\mathscr{D}t(\mathscr{B})$	N–S based approx. for $\mathscr{D}/\mathscr{D}t(\mathscr{A})$ $\mathscr{D}/\mathscr{D}t(\mathscr{B})$	N–S based approx. for $\mathscr{D}/\mathscr{D}t(\mathscr{A})$ and $\mathscr{D}/\mathscr{D}t(\mathscr{B}) = 0$	N–S based approx. for $\mathscr{D}/\mathscr{D}t(\mathscr{B})$ and $\mathscr{D}/\mathscr{D}t(\mathscr{A}) = 0$
Model 2	Unstable	Stable	Unstable	Stable	**Stable**	Unstable
Woods	Unstable	Stable*	Unstable	Stable**	Stable*	Stable**
Model 1	Unstable	Unstable	Stable	Stable	Unstable	Unstable

TABLE 11. A comparison of the stability characteristics of the linearized Model 2 Woods and Model 1 equations for a monatomic hard sphere gas. In this table, $\mathscr{A} = \partial u_x/\partial x$ and $\mathscr{B} = \partial T/\partial x$. The linearized Model 2 equations are stabilized by the Navier–Stokes and steady-state approximations to both the material derivatives. In addition, the Navier–Stokes approximation for $\mathscr{D}/\mathscr{D}t(\mathscr{A})$ and setting $\mathscr{D}/\mathscr{D}t(\mathscr{B}) = 0$ stabilizes the linearized Model 2 equations. These approximations also make the Model 2b equations entropy consistent as indicated by the boldface characters. For an explanation of the * and ** asterisk marks for the approximations see table 6.

the Model 1b coefficients, the non-zero Model 2b, Burnett and Woods coefficients have the same sign. The linearized stability analysis of the Model 2 equations was carried out as described in § 3 and the stability of the Model 1 and Model 2 equations is compared in table 11. It is noted that unlike the Model 1 equations, the Euler approximations to the material derivatives do not stabilize the linearized Model 2 equations. However, it is noticed that the Navier–Stokes and steady-state approximations to both the material derivatives stabilize the linearized Model 2 equations. Also, the Navier–Stokes approximation to $\mathscr{D}/\mathscr{D}t\,(\partial u_x/\partial x)$ and setting the material derivative $\mathscr{D}/\mathscr{D}t\,(\partial T/\partial x) = 0$ stabilizes the linearized Model 2 equations. It is seen that the stability characteristics of the linearized Model 2 and Woods equations are quite similar, save the approximations in the last column in table 11.

7.2. *Applying the entropy-consistent relaxation technique to the Model 2b equations*

The entropy-consistent relaxation technique was applied to the Model 2b equations with the same flow conditions as used earlier (see §§ 4.1 and 6.1). The stable approximations, shown in table 11 were used to evaluate $\dot{\sigma}$ in equation (5.10). Figures 13 and 14 show the variations of $\dot{\sigma}$ for two such approximations for the $M_1 = 5$ shock structure problem on a grid of fineness ratio $\Delta x/\lambda_1 = 0.1$. In figure 13, the

https://doi.org/10.1017/S0022112004007876 Published online by Cambridge University Press

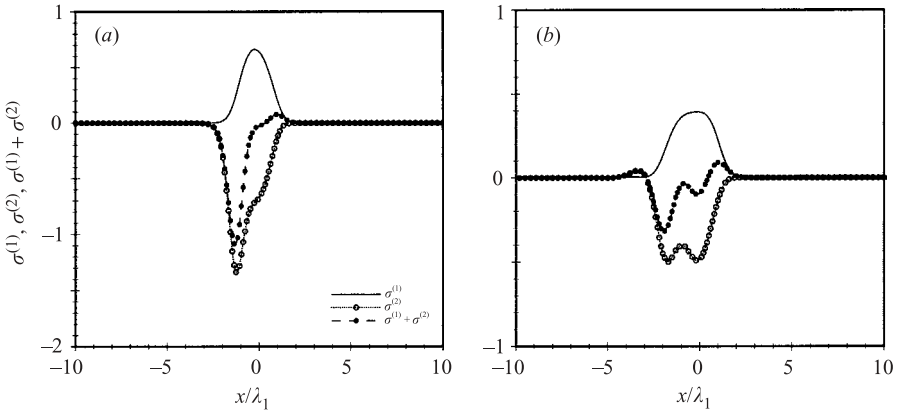


FIGURE 13. Variation of $\dot{\sigma}^{(1)}$, $\dot{\sigma}^{(2)}$ and $\dot{\sigma}^{(1)}+\dot{\sigma}^{(2)}$ for the Model 2b equations for a Mach 5 normal shock, $\Delta x/\lambda_1 = 0.1$. The Navier–Stokes equations were used to approximate $\mathscr{D}/\mathscr{D}t\,(\partial u_x/\partial x)$ and $\mathscr{D}/\mathscr{D}t\,(\partial T/\partial x)$. (*a*) The variations based on a converged Navier–Stokes. (*b*) The same variations based on a Model 2b solution just before the Model 2b equations broke down at this grid fineness ratio.

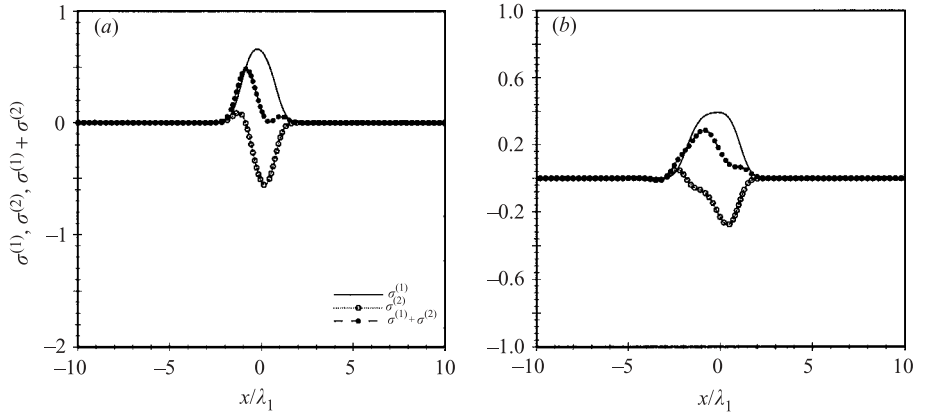


FIGURE 14. Variation of $\dot{\sigma}^{(1)}$, $\dot{\sigma}^{(2)}$ and $\dot{\sigma}^{(1)}+\dot{\sigma}^{(2)}$ for the Model 2b equations for a Mach 5 normal shock, $\Delta x/\lambda_1 = 0.1$. The Navier–Stokes equations were used to approximate $\mathscr{D}/\mathscr{D}t\,(\partial u_x/\partial x)$ and $\mathscr{D}/\mathscr{D}t\,(\partial T/\partial x) = 0$. (*a*) The variations based on a converged Navier–Stokes. (*b*) The same variations based on a Model 2b converged solution. These variations show that the equations are entropy-consistent.

Navier–Stokes approximations were used for both the material derivatives. Starting with an initial shock profile obtained from a converged Navier–Stokes solution, it is seen from figure 13(*a*) that this approximation generates a net negative $\dot{\sigma}$ in the region of the shock. Consequently, when these approximations were used to approximate the material derivatives in the Model 2b flux, it is seen from figure 13(*b*) that the $\dot{\sigma}$ distribution continues to be negative in the region of the shock and the equations break down. However, by using the Navier–Stokes approximation for $\mathscr{D}/\mathscr{D}t\,(\partial u_x/\partial x)$ and setting $\mathscr{D}/\mathscr{D}t\,(\partial T/\partial x) = 0$, it is seen from figure 14 that the $\dot{\sigma}$ variations are positive for the initial shock profile obtained from a converged Navier–Stokes solution and for the converged Model 2b solutions. In figure 14, it is important to note the slight positive peak in $\dot{\sigma}^{(2)}$ in the upstream region of the shock. This peak was not present in the $\dot{\sigma}^{(2)}$ variations obtained from the Model 1b

https://doi.org/10.1017/S0022112004007876 Published online by Cambridge University Press

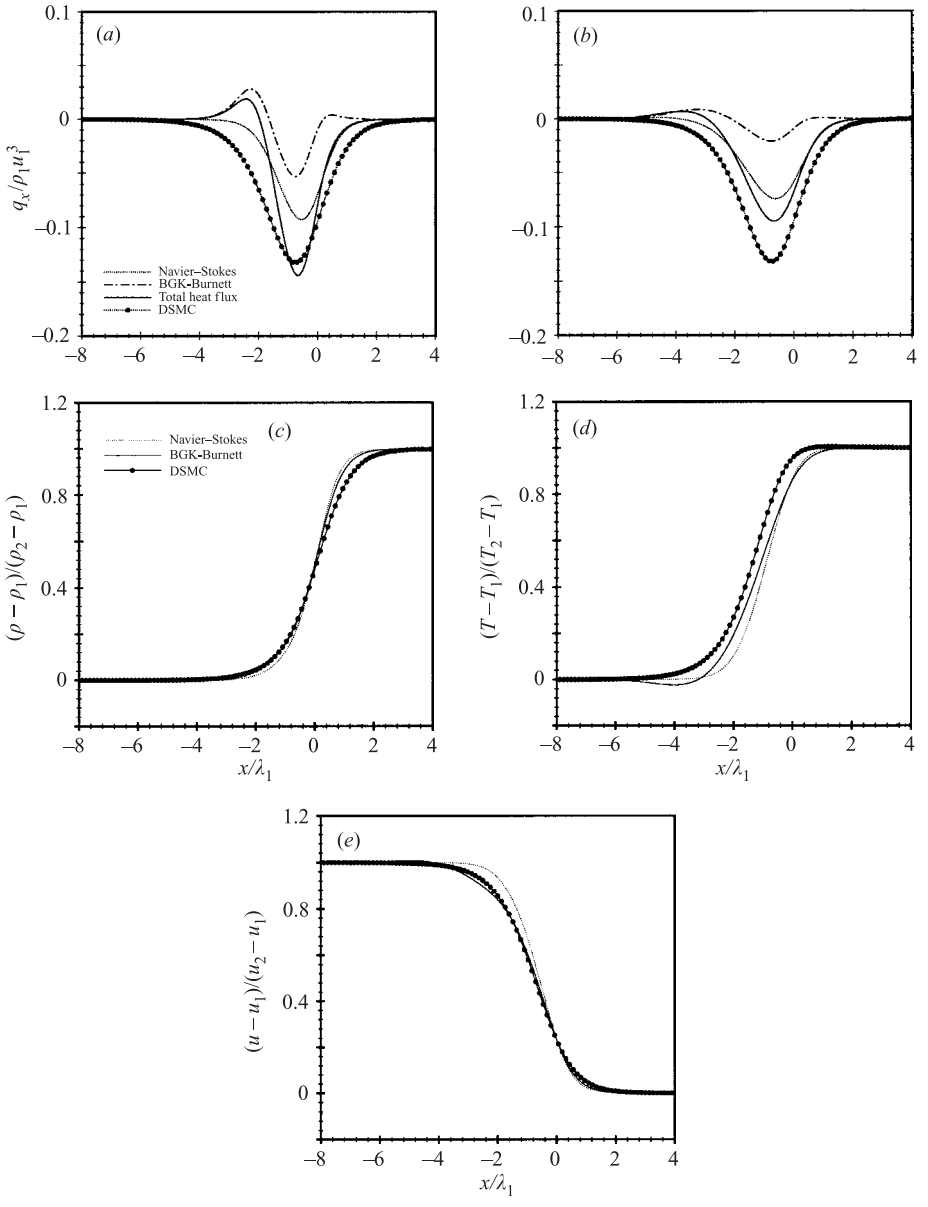


FIGURE 15. (a, b) Comparisons of the variations of the first-order heat flux $\dot{q}_x^v$, the second-order terms $\dot{q}_x^B$ and the total heat flux $\dot{q}_x^v + \dot{q}_x^B$ for the Model 2b equations and DSMC computations for a Mach 5 normal shock in argon gas modelled as a hard sphere gas. (a) The heat flux variations based on a converged Navier–Stokes profile. (b) The heat flux variations based on the converged Model 2b profile. In the second-order flux, the Navier–Stokes equations were used to approximate $\mathscr{D}/\mathscr{D}t\,(\partial u_x/\partial x)$ and $\mathscr{D}/\mathscr{D}t\,(\partial T/\partial x) = 0$. $(c$–$e)$ The variations of the normalized density, temperature and velocity.

solutions. These approximations were, therefore, identified as entropy-consistent approximations to the material derivatives and were used to compute the shock structure for the upstream Mach numbers up to $M_1 = 20$ on a grid of fineness ratio $\Delta x/\lambda_1 = 0.1$. Detailed shock structures for $M_1 = 5$, $M_1 = 10$ and $M_1 = 20$ are shown in

https://doi.org/10.1017/S0022112004007876 Published online by Cambridge University Press

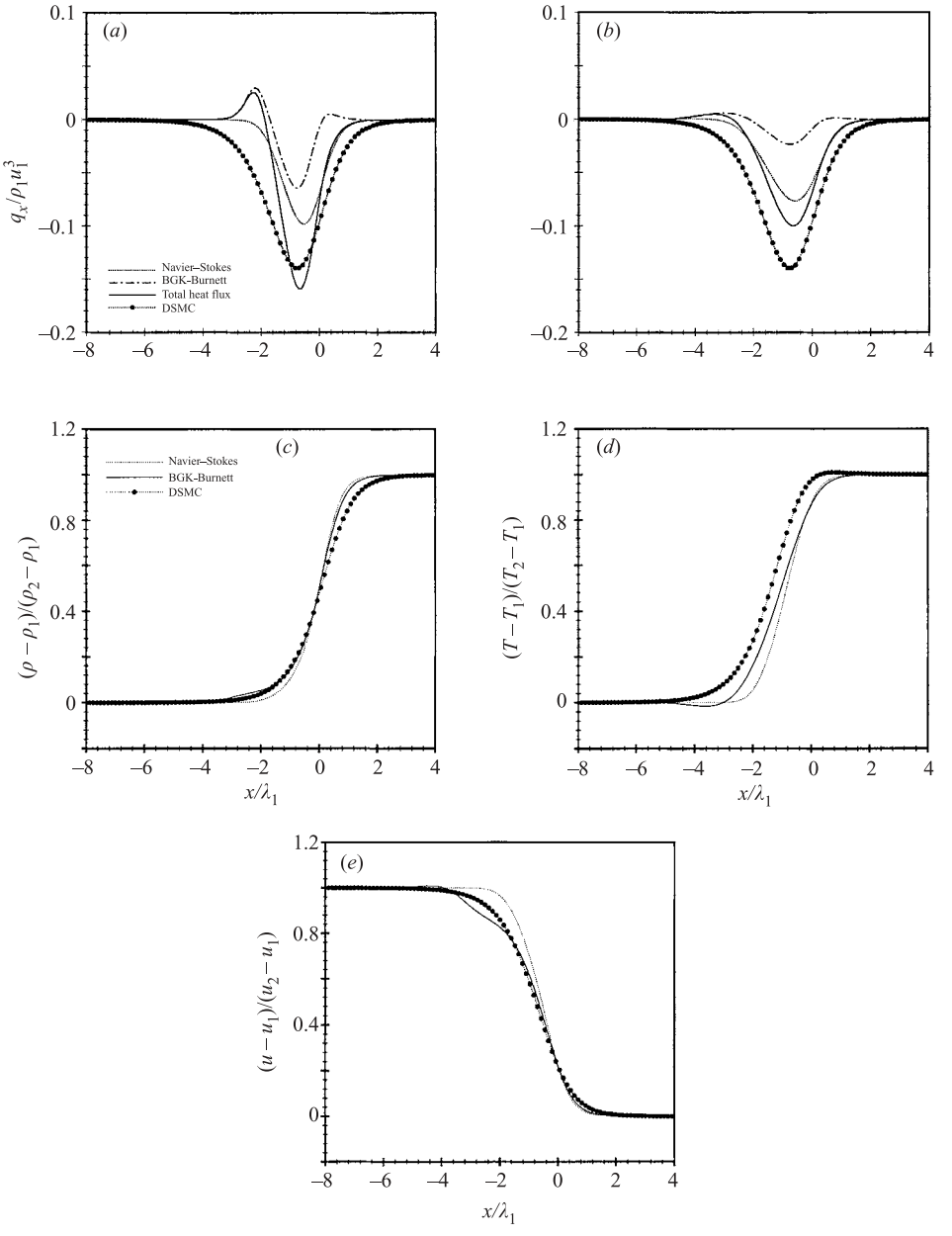


FIGURE 16. As figure 15, but for Mach 10.

figures 15, 16 and 17. The shock profiles of the entropy-consistent Model 2b equations have also been compared with the profiles obtained from DSMC simulations of argon modelled as a hard sphere gas. The DSMC computations were performed with the program DSMC1S.FOR (see Bird 1994) for the same upstream conditions as the Navier–Stokes and Model 2b computations. For the cases considered, the DSMC profiles were obtained after evolving an ensemble of molecules for over 500 million collisions.

https://doi.org/10.1017/S0022112004007876 Published online by Cambridge University Press

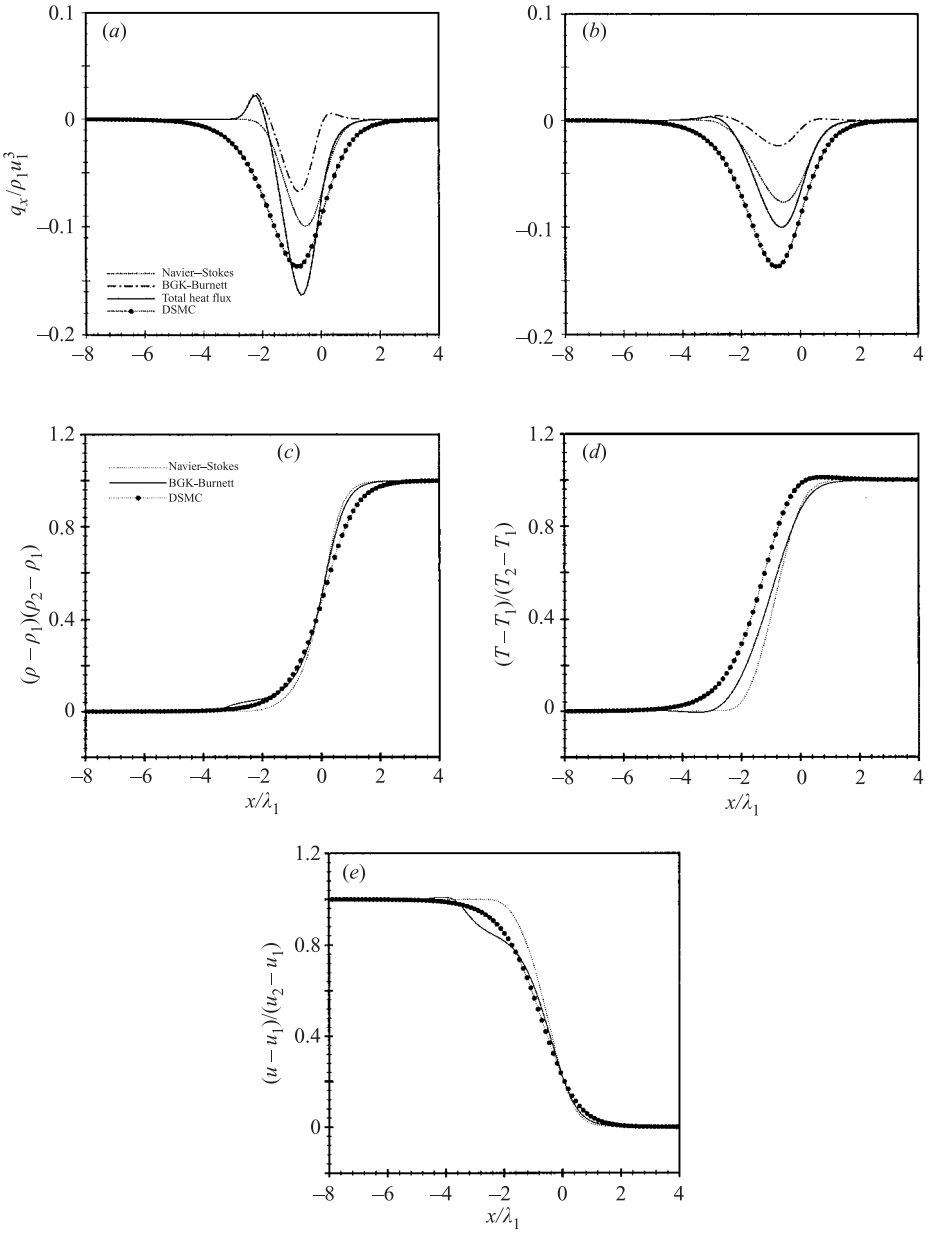


FIGURE 17. As figure 15, but for Mach 20.

From the plot of the heat flux profiles in figures 15(a, b), 16(a, b) and 17(a, b), it can be seen that for the initial shock profile (obtained from a converged Navier–Stokes solution) the Model 2b heat flux creates a positive spike just ahead of the shock. This indicates a heat flux from a cold region, ahead of the shock, to a hot region within the shock. However, as the Model 2b equations relax the initial shock profile, it is noticed that the spike decreases in magnitude, thereby reducing this unphysical transport of thermal energy. Figures 15(c–e), 16(c–e) and 17(c–e) compare the variations of the normalized density, normalized temperature and normalized velocity obtained

https://doi.org/10.1017/S0022112004007876 Published online by Cambridge University Press

from DSMC, Navier–Stokes and Model 2b computations. In plotting the results in figures 15–17 the origin ($x/\lambda_1 = 0$) was chosen as the point where the normalized density is equal to 0.5. There are several points to note in these comparisons. For the $M_1 = 5$, $M_1 = 10$ and $M_1 = 20$ normal shocks, the rise in the normalized density for the DSMC and Model 2b profiles in the upstream region of the shock is in agreement. However, in the downstream region of the shock, the DSMC density profiles spread out more than the Model 2b profiles, thereby increasing the shock thickness. With the temperature profiles it is seen that the DSMC profiles rise ahead of the Model 2b profiles in the upstream region of the shock. The slight positive crest seen in the heat flux profile, in figure 15(*b*), just ahead of the $M_1 = 5$ shock causes the dip in the normalized temperature profile as shown in figure 15(*d*). With an increase in the shock strength it is seen (see figures 16*d* and figure 17*d*) that the positive spike in $\dot{q}_x$ and the dip in the normalized temperature are considerably reduced.

A feature of the solutions of the entropy consistent Model 2b equations is that the normalized density profiles show a hump on the upstream side of the shock profile. The region of this hump increases with shock strength, as seen in the $M_1 = 10$ and $M_1 = 20$ normal shock profiles in figures 16(*c*) and 17(*c*). The computations of the normal shock in argon with the BGK equation (Liepmann, Narasimha & Chahine 1962; Chahine 1963; Chahine & Narasimha 1965) (Boltzmann equation with the BGK model for the collision integral) show a sharp drop in the normalized velocity profiles in the upstream region of the shock. Such a drop is also seen in the normalized velocity profiles of the Model 2b equations as shown in figures 16(*e*) and 17(*e*). The location of this dip corresponds to the rise in the normalized density profiles. This sudden rise in the density profile (and dip in the velocity profile) is not seen in either the experimental density profiles (see Alsmeyer 1976) or the DSMC shock structure computations (see Haviland 1962; Bird 1965). Since this hump is also seen in the $M_1 = 20$ density profile obtained with the augmented Burnett equations for a hard sphere gas (see Zhong 1991) it may be conjectured that this behaviour is not peculiar to the BGK model alone.

For the cases investigated, the shock thickness is computed using the maximum gradients of density, temperature and stress. Although experimental measurements of shock thickness are based on the maximum density gradient, it can be seen from the Model 2b and DSMC computations that the temperature, stress and heat flux profiles indicate a thicker shock. Therefore, the shock thickness is calculated from the following expressions

$$t_\rho = \frac{\rho_2 - \rho_1}{(\partial\rho/\partial x)_{max}}, \quad t_T = \frac{T_2 - T_1}{(\partial T/\partial x)_{max}}, \quad t_{\tau_{xx}} = \frac{\mu_{max}(u_2 - u_1)}{|\tau_{xx}|_{max}} \tag{7.4}$$

and $\max\left(t_\rho, t_T, t_{\tau_{xx}}\right)$ is taken to be the shock thickness. Tables 12 and 13 show the inverse shock thickness calculated from equation (7.4) for the Navier–Stokes and Model 2b profiles. Table 14 compares the inverse shock thickness based on the density gradients with the experimental measurements of Alsmeyer (1976), Camac (1965) and DSMC predictions. It is seen that at low Mach numbers, the Navier–Stokes, Model 2b and DSMC shock thickness are in close agreement. The extrapolated value of the experimental shock thickness, however, indicates a thinner shock. At higher Mach numbers, the Model 2b shock thickness lies in between the Navier–Stokes and DSMC predictions. The experimental measures of the shock thickness, however, indicates a thicker shock than any of the computational predictions. Also, the experimental measures do not level off at high Mach numbers like the computational predictions for a monatomic hard sphere gas.

https://doi.org/10.1017/S0022112004007876 Published online by Cambridge University Press

Upstream Mach number	Inverse Density thickness	Inverse Temperature thickness	Inverse Stress thickness
1.2	6.306×10^{-2}	6.211×10^{-2}	4.825×10^{-2}
5.0	0.576815	0.471664	0.308457
10.0	0.647143	0.526993	0.436082
20.0	0.667823	0.542892	0.439383

TABLE 12. Shock thickness for argon computed using the Navier–Stokes equations. The computed shock thickness measures are based on fine grid solutions, $\Delta x/\lambda_1 = 0.1$.

Upstream Mach number	Inverse Density thickness	Inverse Temperature thickness	Inverse Stress thickness
1.2	6.20585×10^{-2}	6.18614×10^{-2}	9.21306×10^{-3}
5.0	0.503101	0.375218	0.184188
10.0	0.570015	0.405715	0.307753
20.0	0.586499	0.413692	0.308121

TABLE 13. Shock thickness for argon computed using the Model 2b equations. The computed shock thickness measures are based on fine grid solutions, $\Delta x/\lambda_1 = 0.1$.

Upstream Mach number, M_1	Navier–Stokes	BGK-Burnett (Model 2b)	DSMC (hard sphere)	Experimental (Alsmeyer; Camac)
1.2	6.306×10^{-2}	6.20585×10^{-2}	0.06	0.18636
5.0	0.576815	0.503101	0.4	0.261818
10.0	0.647143	0.570015	0.415	0.2227272
20.0	0.667823	0.586499	0.414	N/A

TABLE 14. Comparison of the inverse shock thickness based on density gradients. The Model 2b and Navier–Stokes shock thickness predictions were based on a fine grid solution, $\Delta x/\lambda_1 = 0.1$. The DSMC based inverse shock thickness for argon gas modelled as a hard sphere results compares with the results of Welder *et al.* (1993). The experimental measures of the shock thickness were obtained from Alsmeyer (1976); Camac (1965).

8. Summary and conclusions

The primary objective of this paper was to explore the possibility of formulating a set of entropy-consistent second-order hydrodynamic equations. Towards this end, a novel formulation known as the the BGK-Burnett equations, has been attempted by extending the assumptions made in the formulation of the Navier–Stokes equations to the second-order in the local Knudsen number. The molecules were assumed to collide like 'billiard balls' and the ideal gas equation of state has been assumed. The problems associated with frame dependence have been avoided by confining this formulation to one spatial dimension. In the formulation of the second-order distribution function, the difficulties associated with the highly nonlinear collision integral were circumvented by using the more tractable BGK model equation. The problem of closure has been addressed by solving a set of algebraic equations to determine the moment closure coefficients. These coefficients are, however, not unique and give rise to a family of BGK-Burnett equations. From this family of equations, two sets of BGK-Burnett equations, namely, the Model 1 and Model 2 equations, have been considered to illustrate the formulation of the equations and the ECRT approach to identify approximations to the material derivatives that will make the equations entropy-consistent.

https://doi.org/10.1017/S0022112004007876 Published online by Cambridge University Press

In the formulation of the Model 1a equations, the derivatives of the collision frequency were neglected. This was based on the assumption that the variation in collision frequency across a shock is small – an assumption that is valid only for weak shocks. Although the linearized Model 1a equations were stable with Euler and Navier–Stokes approximations for the material derivatives, an inherent fictitious viscosity, that varied with pressure, made the equations stiff while computing strong shocks with low grid fineness ratios. This caused the Model 1a equations to breakdown on even coarse grids. Including the derivatives of the collision frequency gave the Model 1b equations which have the same stability characteristics as the Model 1a equations. These equations gave solutions on finer grids that indicated thicker shocks than the Navier–Stokes predictions. However, an entropy analysis of the Model 1b solutions showed that there was negative irreversible entropy production – a clear violation of the second law of thermodynamics.

The Model 2 equations were formulated by requiring that the linearized BGK-Burnett and Navier–Stokes equations have similar stability trajectories. By applying the ECRT it was found that the Navier–Stokes approximation to $\mathscr{D}/\mathscr{D}t\,(\partial u_x/\partial x)$ and setting $\mathscr{D}/\mathscr{D}t\,(\partial T/\partial x) = 0$ gave a set of Model 2b equations that are stable and entropy-consistent. These equations were used to compute the shock structures for a monatomic hard sphere gas for upstream Mach numbers up to $M_1 = 20$ on a grid of fineness ratio $\Delta x/\lambda_1 = 0.1$. A comparison of the Model 2b density profiles with those obtained from DSMC computations shows that there is good agreement on the upstream side of the shock. However, the DSMC density profiles are more spread out in the downstream region, thereby adding to the shock thickness. The DSMC temperature profiles rise ahead of the Model 2b profiles for all the strong shock structures considered in this study. These differences notwithstanding, it has been shown that by using the ECRT it is possible to identify an entropy-consistent set of second-order equations from the family of BGK-Burnett equations.

The development of the BGK-Burnett equations forms part of the author's doctoral dissertation and the author would like to thank Professor Ramesh K. Agarwal for providing the opportunity to pursue this research at Wichita State University and the National Institute of Aviation Research, Wichita, Kansas. The author is grateful to Professor G. A. Bird for providing the DSMC computer program to compute the DSMC shock profiles. The author would like to thank Professor Philip L. Varghese and Mr Ju Zhang for clarifications regarding the various parameters in the program DSMC1S.FOR. The author would also like to thank Professor Alejandro Garcia for helpful discussions regarding DSMC computations. Special thanks are due to the referees of this paper for their insightful comments and constructive criticisms; many of which motivated revisions to the initial draft. The author would also like to acknowledge the encouragement, financial support and computational facilities provided by the Center for Simulation of Advanced Rockets at the University of Illinois at Urbana–Champaign.

REFERENCES

Abe, T. & Oguchi, H. 1977 A hierarchy kinetic model and its applications. In *Progress in Aeronautics and Astronautics*, vol. 51, pp. 781–806. AIAA.

Agarwal, R. K., Yun, K.-Y. & Balakrishnan, R. 2001 Beyond Navier–Stokes: Burnett equations for flows in the continuum–transition regime. *Phys. Fluids* **13**, 3061–3085.

Al-Ghoul, M. & Eu, B. C. 2001 Generalized hydrodynamics theory of shock waves in rigid diatomic gases. *Phys. Rev.* E **64**, 046303–1 – 046303–2.

https://doi.org/10.1017/S0022112004007876 Published online by Cambridge University Press

Alsmeyer, H. 1976 Density profiles in argon and nitrogen shock waves measured by the absorption of an electron beam. *J. Fluid Mech.* **74**, 497–513.

Balakrishnan, R. 1999 Entropy consistent formulation and numerical Simulation of the BGK-Burnett equations for hypersonic flows in the continuum-transition regime. PhD thesis, Wichita State University.

Balakrishnan, R. & Agarwal, R. K. 1997 Numerical simulation of Bhatnagar–Gross–Krook Burnett equations for hypersonic flows. *J. Thermophys. Heat Transfer* **11**, 391–399.

Balakrishnan, R., Agarwal, R. K. & Yun, K. Y. 1999 BGK-Burnett equations for flows in the continuum–transition regime. *J. Thermophys. Heat Transfer* **13**, 397–410.

Bhatnagar, P. L. 1954 A model for collisional processes in gases. I. Small amplitude processes in charged and neutral one-component systems. *Phys. Rev.* **94**, 511–525.

Bird, G. A. 1965 Shock wave structure in a rigid sphere gas. In *Rarefied Gas Dynamics*, vol. 1, pp. 216–222. Academic.

Bird, G. A. 1994 *Molecular Gas Dynamics and the Direct Simulation of Gas Flows*. Oxford University Press.

Bobylev, A. V. 1982 The Chapman-Enskog and Grad methods for solving the Boltzmann equation. *Sov. Phys. Dokl.* **27**(1), 29.

Boyd, I. D., Chen, G. & Candler, G. V. 1995 Predicting failure of the continuum fluid equations in transitional hypersonic flows. *Phys. Fluids* **7**, 210–219.

Camac, M. 1965 Argon shock structure. In *Rarefied Gas Dynamics*, vol. 1, pp. 240–249. Academic.

Chahine, M. T. 1963 The structure of strong shock waves in the Krook Collision model. In *Rarefied Gas Dynamics*, vol. 1, pp. 260–273. Academic.

Chahine, M. T. & Narasimha, R. 1965 Exact numerical solution of the complete BGK equation for Strong shock waves. In *Rarefied Gas Dynamics*, vol. 1, pp. 140–160. Academic.

Chapman, S. & Cowling, T. G. 1970 *The Mathematical Theory of Non-Uniform Gases*. Cambridge University Press.

Comeaux, K. A. 1995 An evaluation of the second order constitutive relations for rarefied gas dynamics based on the second law of thermodynamics. PhD thesis, Stanford University.

Deshpande, S. M. 1986 On the Maxwellian distribution, symmetric form and entropy conservation for the Euler equations. TR 2583. NASA.

Fiscko, K. A. & Chapman, D. R. 1988 Comparison of the Burnett, super-Burnett and Monte-Carlo solutions for hypersonic shock structure. In *16th Intl Symp. of Rarefied Gas Dynamics*.

ter Haar, D. 1956 *Elements of Statistical Mechanics*, pp. 331–385. Butterworth Heinemann.

Haviland, J. K. 1962 Determination of shock wave thickness by the Monte Carlo method. In *Rarefied Gas Dynamics*, pp. 274–295. Academic.

Holway, L. H. 1965 Kinetic theory of shock structure using an ellipsoidal distribution function. In *Rarefied Gas Dynamics*, vol. 1, pp. 193–215. Academic.

Jin, S., Pareschi, L. & Slemrod, M. 2002 A relaxation scheme for solving the Boltzmann equation based on the Chapman–Enskog expansion. *Acta Math. Applic. Sinica English Scr.* **18**, 37–62.

Jin, S. & Slemrod, M. 2001 Regularization of the Burnett equations via relaxation. *Physica* D **150**, 207–218.

Liepmann, H. W., Narasimha, R. & Chahine, M. T. 1962 Structure of a plane shock layer. *Phys. Fluids* **5**, 1314–1324.

Lumpkin, F. E. 1990 Development and evaluation of continuum models for translational-rotational nonequilibrium. PhD thesis, Stanford University.

Moss, J. N. & Bird, G. A. 1984 Direct simulation of transitional flows for hypersonic reentry conditions. AIAA-84-0223.

Muller, I. 1972 On the frame dependence of stress and heat flux. *Arch. Rat. Mech. Anal.* **45**, 241–250.

Rao, S. V. R. & Deshpande, S. M. 1995 Peculiar velocity based upwind method for inviscid compressible flows. *CFD J. Japan Soc. CFD* **3**, 415–432.

Reese, J. M., Woods, L. C., Thivet, F. J. P. & Candel, S. M. 1995 A second-order description of shock structure. *J. Comput. Phys.* **117**, 240–250.

Vincenti, W. G. & Kruger, C. H. 1965 *Introduction to Physical Gas Dynamics*. Krieger Malabar, FL.

Welder, W. T., Chapman, D. R. & MacCormack, R. W. 1993 Evaluation of the various forms of the Burnett equations. AIAA-93-3094.

https://doi.org/10.1017/S0022112004007876 Published online by Cambridge University Press

Woods, L. C. 1993 *An Introduction to the Kinetic Theory of Gases and Magnetoplasmas*. Oxford University Press.

Yun, K. Y., Agarwal, R. K. & Balakrishnan, R. 1997 A comparative study of augmented Burnett and BGK-Burnett equations for computing hypersonic blunt body flows. AIAA-97-0980.

Zhong, X. 1991 Development and computation of continuum higher-order constitutive relations for high-altitude hypersonic flows. PhD thesis, Stanford University.

Zhong, X. & Furumoto, G. H. 1995 Augmented Burnett-equation solutions over axisymmetric blunt bodies in hypersonic flow. *J. Spacecraft Rockets* **32**, 588–595.

https://doi.org/10.1017/S0022112004007876 Published online by Cambridge University Press